PERGAMON

Computers and Structures 80 (2002) 769–789

Computers & Structures

www.elsevier.com/locate/compstruc

A stabilized MITC element for accurate wave response in Reissner–Mindlin plates ☆

Lonny L. Thompson *, Sri Ramkumar Thangavelu

Department of Mechanical Engineering, Clemson University, 102 Fluor Daniel Engineering Innovation Building, Clemson, SC 29634-0921, USA

Accepted 1 February 2002

Abstract

Residual based finite element methods are developed for accurate time-harmonic wave response of the Reissner–Mindlin plate model. The methods are obtained by appending a generalized least-squares term to the mixed variational form for the finite element approximation. Through judicious selection of the design parameters inherent in the least-squares modification, this formulation provides a consistent and general framework for enhancing the wave accuracy of mixed plate elements. In this paper, the mixed interpolation technique of the well-established MITC4 element is used to develop a new mixed least-squares (MLS4) four-node quadrilateral plate element with improved wave accuracy. Complex wave number dispersion analysis is used to design optimal mesh parameters, which for a given wave angle, match both propagating and evanescent analytical wave numbers for Reissner–Mindlin plates. Numerical results demonstrates the significantly improved accuracy of the new MLS4 plate element compared to the underlying MITC4 element.

Keywords: Finite element methods; Reissner–Mindlin plates; Mixed interpolation; Plate elements; Shell elements

1. Introduction

When modeling the time-harmonic response of elastic structures, accurate plate and shell elements are needed to resolve both propagating and evanescent waves over a wide range of frequencies and scales. The propagating waves are characterized by sinusoidal components with phase speed determined by the material properties and thickness of the plate, while the evanescent waves are characterized by exponential decay with effects localized near drivers and discontinuities, e.g., near boundary layers. Models based on classical Kirchhoff plate theory agree with the exact theory of elasticity only in a very limited low range of frequencies; the predicted phase speed at higher frequencies is infinite, while the exact theory remains bounded [2]. The inclusion of transverse shear deformation and rotary inertia effects in the Reissner–Mindlin theory accuracy predicts the bounded phase speed of the exact theory over a large range of frequencies of typical interest [4–6]. The accuracy improvement for intermediate to high frequencies plays an important role in modeling control–structure interactions, dynamic localizations, acoustic fluid–structure interaction, scattering from inhomogeneities, and other applications requiring precise modeling of dynamic characteristics.

The numerical solution of the Reissner–Mindlin plate model for static analysis has been discussed by many authors, e.g. [7–13]. The primary focus has been various remedies to the well-known shear locking problem for very thin plates, [14,15]. The locking is most clearly seen in some low order approximations where an overly stiff response to bending is exhibited in the solution.

☆ Portions of this manuscript originally presented in [1].

* Corresponding author. Tel.: +1-864-656-5631; fax: +1-864-656-4435.

E-mail address: lonny.thompson@ces.clemson.edu (L.L. Thompson).

0045-7949/02/$ - see front matter
PII: S0045-7949(02)00046-9

Mathematically, the locking is the result of the lack of stability of the method. Over the last decade, significant progress has been made on the mathematical stability and error analysis for Reissner–Mindlin plate elements for static analysis [16–28]. Of the low order elements, the popular bilinear MITC4 element [9] based on mixed interpolation of shear strains is one of the most attractive. Later, Prathap [10] rederived the same four-node quadrilateral plate element using the concepts of field- and edge-consistency. The error analysis [16,17] performed on this element showed that it is optimally convergent for deflections and rotations on regular meshes. However, for the four-node quadrilateral MITC4 element, it is not clear what is the optimal definition of the loading and mass which is consistent with the assumed strain field for dynamic analysis. While eliminating shear locking problems for thin plates, what is often overlooked is the large dispersion error exhibited in these elements leading to inaccurate resolution of propagating and evanescent wave behavior in dynamic analysis at intermediate to high frequencies.

To address this problem, a residual-based modification of assumed strain mixed methods for Reissner–Mindlin plates is proposed. New plate elements are developed based on a generalized least-squares modification to the total energy for the time-harmonic Reissner–Mindlin plate model. The least-squares operators are proportional to residuals of the governing equations of motion, and provide a consistent framework for enhancing the wave accuracy of Reissner–Mindlin plate elements for forced vibration and time-harmonic response. Any of several existing mixed finite element interpolation fields which yield plate elements which are free from shear locking and pass the static patch test may be used. Here we start from the firm mathematical foundation inherent in the shear projection technique of the MITC4 element. A similar generalized least-squares approach was used in [29,30,32] to improved the accuracy of quadrilateral plate elements based on assumed stress fields in a modified Hellinger–Reissner variational principle.

Weighted residuals of the governing Euler–Lagrange equations in least-squares form were first used to stabilize the pathologies exhibited by the classical Galerkin method for the numerical solution of advection–diffusion problems [33]. These so-called stabilized methods have been successfully employed in a wide variety of applications where enhanced stability and accuracy properties are needed, including problems governed by Navier–Stokes and the compressible Euler equations of fluid mechanics, [34]. Generalized methods based on the gradient of the residuals in least-squares form were first used by Franca and do Carmo [35] for the advection–diffusion equation. In [36,37], Hughes et al. established a relationship between various stabilized methods and variational multiscale methods. Residual-based methods have since been extended to the scalar Helmholtz equation governing steady-state vibration and time-harmonic wave propagation, (e.g. acoustics), by Harari and Hughes, [38,39], and Thompson and Pinsky [40]. In [40,41], finite element dispersion analysis was used to select mesh parameters in the least-squares modification to the Galerkin method, resulting in improved phase accuracy for both two- and three-dimensional problems. In Oberai and Pinsky [42], variable mesh parameters and residuals on inter-element boundaries are included to reduce the directional dependence of dispersion error. Other numerical methods designed to improve the accuracy of the scalar Helmholtz equation can be found in e.g. [43,44].

The first use of residual based methods for static analysis of plate structures was the stabilized mixed formulations by Hughes and Franca [20] where symmetric forms of the equilibrium equations were appended to the standard Galerkin equations to improve transverse shear accuracy. In [27], the stabilized formulations of [20] are combined with the shear interpolation of the MITC plate bending element for static analysis. Grosh and Pinsky applied a generalization of the Galerkin gradient least squares (GGLS) method of Franca and do Carmo [35] to improve the accuracy of displacement based Timoshenko beam elements for steady-state vibration [45]. An important feature of this GGLS element, is that in the zero frequency limit, the mesh parameters modify the shear strain approximation in the stiffness matrix, reverting to selective-reduced-integration (SRI) in the static case. As mentioned in [45], the extension of this GGLS formulation for 1-D Timoshenko beams to 2-D Reissner–Mindlin plate elements based on bilinear displacement interpolation failed to produce a quadrilateral element which is free from shear locking.

In this work, we combine the mixed interpolation of the MITC4 plate element with residual-based methods to develop a mixed least squares (MLS) quadrilateral element for accurate time-harmonic wave response of the Reissner–Mindlin plate model. A key feature of our method is that we require the mesh parameters to vanish in the static limit of zero frequency, thus retaining the locking-free behavior of the underlying MITC quadrilateral element. Using complex wave number dispersion analysis [46], we design optimal mesh parameters, which, for a given wave angle relative to a uniform finite element mesh, match both propagating and evanescent analytic wave numbers for Reissner–Mindlin plates. This strategy for designing mesh parameters is similar to that used in the displacement based GGLS Timoshenko beam element proposed in [45], here extended to arbitrary quadrilateral plates. In general, the direction of wave propagation is not known a priori. However, similar to [40], we can select a wave angle in the definitions for the mesh parameters to minimize dispersion error over the entire range of possible angles.

2. Reissner–Mindlin plate equations

We consider the Reissner–Mindlin plate bending model [4–6] with thickness t, two-dimensional midsurface $A \subset \mathbb{R}^2$, boundary ∂A, and transverse coordinate z. The distributed load $q(x,y)$ is restricted to the direction normal to the midsurface defined by the unit vector $\boldsymbol{e}_z$. Without loss of generality, we assume that the plate is clamped along its boundary. The deformation at any point is given by the three-dimensional displacement vector defined by

$$\boldsymbol{u} = -z\boldsymbol{\theta}(x,y) + w(x,y)\boldsymbol{e}_z, \tag{1}$$

where $\boldsymbol{\theta} = [\theta_x, \theta_y]^{\mathrm{T}} \in [H_0^1(A)]^2$ denotes the two-dimensional vector of section rotations, such that $\boldsymbol{\theta} \perp \boldsymbol{e}_z$, and $w \in H_0^1(A)$ is the vertical deflection of the midsurface. The components θ_x and θ_y are the section rotations about the y and x axes respectively. As a consequence of the kinematic assumptions, the in-plane bending strain tensor $\boldsymbol{\varepsilon} = -z\boldsymbol{\kappa}$, is linearly related to the tensor of curvatures $\boldsymbol{\kappa}$, through the symmetric part of the rotation gradient,

$$\boldsymbol{\kappa}(\boldsymbol{\theta}) := \tfrac{1}{2}(\nabla\boldsymbol{\theta} + (\nabla\boldsymbol{\theta})^{\mathrm{T}}). \tag{2}$$

Using first-order shear deformation theory, the transverse shear strains are defined by the angle between the slope of the midsurface after deformation and the section angle, $\gamma = \nabla w - \boldsymbol{\theta}$.

For a homogeneous, isotropic plate with linear elastic material properties, the constitutive relations for the bending moment and shear resultants are

$$\boldsymbol{M} = \frac{EI}{(1+\nu)}\left\{\boldsymbol{\kappa}(\boldsymbol{\theta}) + \left(\frac{\nu}{1-\nu}\right)(\operatorname{div}\boldsymbol{\theta})\boldsymbol{I}\right\}, \tag{3}$$

$$\boldsymbol{Q} = G_s t(\nabla w - \boldsymbol{\theta}). \tag{4}$$

Here, $I = t^3/12$, with Young's modulus E, Poisson's ratio ν, shear modulus G, and κ is a shear correction factor, $G_s = \kappa G$. In the above, 'div' stands for divergence, i.e., $\operatorname{div}\boldsymbol{\theta} = \theta_{x,x} + \theta_{y,y}$, and $\boldsymbol{I}$ is the unit tensor.

We assume time-harmonic motion with time-dependence $\mathrm{e}^{-\mathrm{i}\omega t}$; ω is the circular frequency measured in rad/s. The variational problem is to minimize the total energy functional with respect to the generalized displacements $\boldsymbol{v} = (w, \boldsymbol{\theta})$. For the Reissner–Mindlin model, the total energy may be expressed as

$$F_{\mathrm{M}}(\boldsymbol{v}) = \Pi_{\mathrm{M}}(\boldsymbol{v}) - \omega^2\frac{1}{2}\int_A [\rho t(w)^2 + \rho I(\boldsymbol{\theta})^2]\,\mathrm{d}A - \int_A wq\,\mathrm{d}A. \tag{5}$$

In the above, ρt is the mass density per unit area, ρI is the rotary inertia, Π_{M} is the internal strain energy split into bending and shear parts

$$\Pi_{\mathrm{M}}(\boldsymbol{v}) = \frac{1}{2}B(\boldsymbol{\theta},\boldsymbol{\theta}) + \frac{G_s t}{2}\int_A (\nabla w - \boldsymbol{\theta})^2\,\mathrm{d}A, \tag{6}$$

$$B(\boldsymbol{\theta},\boldsymbol{\theta}) := \frac{EI}{(1+\nu)}\int_A \left[\boldsymbol{\kappa}(\boldsymbol{\theta}) : \boldsymbol{\kappa}(\boldsymbol{\theta}) + \left(\frac{\nu}{1-\nu}\right)(\operatorname{div}\boldsymbol{\theta})^2\right]\mathrm{d}A. \tag{7}$$

The symmetric tensor inner product is defined by, $\boldsymbol{\kappa}$: $\boldsymbol{\kappa} = \kappa_x^2 + \kappa_y^2 + 2\kappa_{xy}^2$.

The dynamic Euler–Lagrange equations corresponding to this variational problem are:

$$R_1 := \operatorname{div}\boldsymbol{Q} + (\rho t\omega^2)w + q = 0, \tag{8}$$

$$\boldsymbol{R}_2 := \operatorname{div}\boldsymbol{M} + \boldsymbol{Q} + (\rho I\omega^2)\boldsymbol{\theta} = \boldsymbol{0}, \tag{9}$$

In the above, R_1 is a scalar residual associated with shear equilibrium, and $\boldsymbol{R}_2 = [R_{2x}, R_{2y}]^{\mathrm{T}}$ is a vector residual associated with moment equilibrium. Applying the divergence operator to the vector Eq. (9), i.e. $\operatorname{div}\boldsymbol{R}_2$, and writing the bending and shear resultants in terms of displacements $\boldsymbol{M} = \boldsymbol{M}(\boldsymbol{\theta})$ and $\boldsymbol{Q} = \boldsymbol{Q}(w,\boldsymbol{\theta})$, via (3) and (4), the residuals can be restated in terms of the two scalar equations,

$$R_1(\boldsymbol{v}) := D_s\operatorname{div}\gamma + (\rho t\omega^2)w + q = 0 \tag{10}$$

$$R_2(\boldsymbol{v}) := \operatorname{div}\boldsymbol{R}_2 = \left(D_b\nabla^2 + \rho I\omega^2\right)\operatorname{div}\boldsymbol{\theta} + D_s\operatorname{div}\gamma = 0 \tag{11}$$

where $D_b = EI/(1-\nu^2)$, $D_s = G_s t$, $\nabla^2 = \operatorname{div}\nabla$, and $\gamma = \nabla w - \boldsymbol{\theta}$.

2.1. Wave number–frequency dispersion relation

The homogeneous plate equations of motion admit solutions of the form

$$w = w_0\mathrm{e}^{(\mathrm{i}k\boldsymbol{v}\boldsymbol{x})}, \quad \boldsymbol{\theta} = \theta_0\boldsymbol{v}\mathrm{e}^{(\mathrm{i}k\boldsymbol{v}\boldsymbol{x})}, \quad \operatorname{div}\boldsymbol{\theta} = \mathrm{i}k\theta_0\mathrm{e}^{(\mathrm{i}k\boldsymbol{v}\boldsymbol{x})} \tag{12}$$

In the above, $i = \sqrt{-1}$, k is the wave number, $\boldsymbol{v} = [\cos\varphi, \sin\varphi]$ defines a unit vector in the direction of wave propagation, with wave vector $\boldsymbol{k} = k\boldsymbol{v} = k[\cos\varphi, \sin\varphi]$. Conditions for the allowed waves are obtained by substituting the assumed exponentials (12) into the homogeneous equations of motion (10) and (11) with $q = 0$. The result is the dispersion equation relating frequency ω to wave number k:

$$\mathscr{D}(k,\omega) := k^4 - (k_s^2 + k_p^2)k^2 + (k_p^2k_s^2 - k_b^4) = 0, \tag{13}$$

$$k_p = \omega/c_p, \quad k_s = \omega/c_s, \quad k_b = (\rho t\omega^2/D_b)^{1/4},$$

$$c_p = \left[\frac{E}{\rho(1-\nu^2)}\right]^{1/2}, \quad c_s = \left(\frac{G_s}{\rho}\right)^{1/2}.$$

Wave number solutions occur in pairs: $\pm k_1$ and $\pm k_2$. The character of these solutions are well known [2,3]. At

frequencies below a cut-off frequency, the wave number pair $\pm k_1$ occurs as purely real, while the pair $\pm k_2$ is purely imaginary. The real wave number pair corresponds to propagating waves while the imaginary pair corresponds to evanescent waves characterized by exponential decay.

3. Generalized finite element formulation

Consider a finite element mesh obtained by partitioning A into convex quadrilateral elements. Let A_e denote the area for a typical element number e. We then define $\mathscr{M}_h = \cup_e A_e$ as the union of element interiors. The discrete total energy for the plate equations of motion with assumed strain γ^h and trial displacements $\boldsymbol{v}^h = (w^h, \boldsymbol{\theta}^h)$ may be stated as

$$F_{\mathrm{M}}(\boldsymbol{v}^h) := \Pi_{\mathrm{M}}(\boldsymbol{v}^h) - \omega^2 \frac{1}{2}\int_A \left[\rho t (w^h)^2 + \rho I(\boldsymbol{\theta}^h)^2\right] \mathrm{d}A - \int_A w^h q \,\mathrm{d}A, \tag{14}$$

$$\Pi_{\mathrm{M}}(\boldsymbol{v}^h) = \frac{1}{2} B(\boldsymbol{\theta}^h, \boldsymbol{\theta}^h) + \frac{G_s t}{2}\int_A (\gamma^h)^2 \,\mathrm{d}A. \tag{15}$$

Remark. The variational equations associated with the above functional with the kind of interpolations described in the following section, should also include the shear force resultants $\boldsymbol{Q}^h$ as additional dependent variables [19]. However, imposing an orthogonality condition [19], the shear force is eliminated from the final form.

To develop a residual-based formulation with enhanced wave number accuracy, we start with the total energy functional and then add weighted differential least-squares operators proportional to the governing dynamic equations of motion. Our modified functional can be written as

$$F_{\mathrm{MLS}}(\boldsymbol{v}^h) = F_{\mathrm{M}}(\boldsymbol{v}^h) + F_{\mathrm{LS}}(\boldsymbol{v}^h) \tag{16}$$

with generalized least-squares term,

$$F_{\mathrm{LS}}(\boldsymbol{v}^h) = \frac{1}{2}\sum_{A_e \in \mathscr{M}_h} \int_{A_e} \left\{\tau_1 (\nabla R_1^h)^2 + \tau_2 (R_2^h)^2\right\} \mathrm{d}A. \tag{17}$$

In the above,

$$R_1^h = D_s \mathrm{div}\,\gamma^h + \rho t \omega^2 w^h + q, \tag{18}$$

$$R_2^h = \mathrm{div}\,\boldsymbol{R}_2^h = \left(D_b \nabla^2 + \rho I \omega^2\right)\mathrm{div}\,\boldsymbol{\theta}^h + D_s \mathrm{div}\,\gamma^h \tag{19}$$

are discrete residual functions for the dynamic plate equations. The functions $\tau_1(\omega)$ and $\tau_2(\omega)$ are frequency dependent local mesh parameters determined from dispersion analysis and designed to match the analytical wave number–frequency relation for Mindlin plates. Setting $\tau_1 = \tau_2 = 0$, reverts to the underlying assumed strain formulation. The residual-based least-squares terms are constructed to maintain symmetry of the underlying energy functional for isotropic materials. The use of derivatives on the residuals is necessary to simplify the formulation for elements with low-order approximations.

A slightly simplified form results if we neglect a cross-coupling term $(R_{2x,x}R_{2y,y})$, resulting in the alternative form,

$$F_{\mathrm{LS}}(\boldsymbol{v}^h) = \frac{1}{2}\sum_{A_e \in \mathscr{M}_h} \int_{A_e} \left\{\tau_1 (\nabla R_1^h)^2 + \tau_2 \left[\left(R_{2x,x}^h\right)^2 + \left(R_{2y,y}^h\right)^2\right]\right\} \mathrm{d}A. \tag{20}$$

Both forms (17) and (20) may be recast in a more general expression for the least-squares operator, see [31]. Any of several existing mixed finite element approximation fields which give rise to spaces which avoid shear locking and pass the static patch test may be used with either least-squares functional (17) or (20). In this paper, we use the field- and edge-consistent interpolations of the popular MITC4 plate bending element originally proposed by Bathe and Dvorkin [9]. In [30], least-square stabilizing operators similar to (20), but with residuals defined by *independent* moment and shear resultants, were used to modify the discrete Hellinger–Reissner functional in an assumed stress hybrid element formulation. The difference here is that the stress resultants are written as *dependent* functions of generalized displacements and assumed shear strains.

In the following, we denote four-node quadrilateral elements based on the functional forms (17) and (20) as MLS4-1 and MLS4-2, respectively.

3.1. Finite element interpolations

We define the finite element subspaces for the approximation of the deflection w^h and rotation vector $\boldsymbol{\theta}^h$ as

$$W_h = \left\{w^h \in H_0^1(A), w^h|_{A_e} \in Q_1[A_e], \forall A_e \in \mathscr{M}_h\right\}, \tag{21}$$

$$\boldsymbol{V}_h = \{\boldsymbol{\theta}^h \in H_0^1(A), \boldsymbol{\theta}^h|_{A_e} \in [Q_1(A_e)]^2, \forall A_e \in \mathscr{M}_h\}, \tag{22}$$

where $Q_1(A_e)$ is the set of low-order polynomials of degree $\leqslant 1$ in each variable defined on A_e, and A_e is the current element in the discretization. This space of polynomials provides for equal order basis functions for the deflection and both components of the rotation. The finite element interpolation of the element domain A_e, together with the displacement field w^h, and $\boldsymbol{\theta}^h$, follows the standard isoparametric procedure [14]. We define $\boldsymbol{\xi} = (\xi, \eta)$ to be natural coordinates on the reference biunit square $\hat{A}$ defined by the interval $[-1, 1]^2$. The

reference domain is then mapped onto the physical element domain A_e with cartesian coordinates $\boldsymbol{x} = (x, y)$ parameterized by,

$$\boldsymbol{x}(\xi,\eta) = \sum_{i=1}^{4} N_i(\xi,\eta)\boldsymbol{x}_i, \tag{23}$$

where $\boldsymbol{x}_i = (x_i, y_i) \in \mathbb{R}^2$ are nodal coordinates, and N_i are bilinear shape functions,

$$N_i(\xi,\eta) = (1+\xi_i\xi)(1+\eta_i\eta)/4, \quad i = 1,\ldots,4 \tag{24}$$

with nodal coordinates $(\xi_i,\eta_i) \in \{(-1,-1);\ (1,-1);\ (1,1);\ -1,1)\}$. The displacements are constructed using the same bilinear functions:

$$w^h(\xi,\eta) = \sum_{i=1}^{4} N_i(\xi,\eta)w_i, \quad \boldsymbol{\theta}^h(\xi,\eta) = \sum_{i=1}^{4} N_i(\xi,\eta)\boldsymbol{\theta}_i, \tag{25}$$

where w_i are nodal deflections and $\boldsymbol{\theta}_i = [\theta_x^i, \theta_y^i]$, are nodal rotations. We let $[\boldsymbol{J}]$ be the Jacobian transformation matrix of the mapping $\boldsymbol{x}$: $\hat{\boldsymbol{A}} \to A_e$, i.e. $\hat{\nabla} = [\boldsymbol{J}]^{\mathrm{T}}\nabla$, where

$$[\boldsymbol{J}] := [\boldsymbol{x}_{,\xi}] = \begin{bmatrix} x_{,\xi} & x_{,\eta} \\ y_{,\xi} & y_{,\eta} \end{bmatrix}. \tag{26}$$

Here $\hat{\nabla}$ stands for the gradient operator with respect to the ξ and η variables.

3.2. Assumed shear strain field

To eliminate locking, the shear energy is defined in terms of the assumed covariant transverse shear strain field of the MITC4 mixed interpolation [9]. The assumed strain γ^h is defined by a reduction operator $\boldsymbol{R}_h : [H^1(A_e)]^2 \to \boldsymbol{\Gamma}_h(A_e)$, which maps the shear strain interpolants evaluated from the spaces W^h and $\boldsymbol{V}^h$ to the assumed strain space $\boldsymbol{\Gamma}_h$, [16–18], i.e.,

$$\begin{aligned}\gamma^h &= \boldsymbol{R}_h(\nabla w^h - \boldsymbol{\theta}^h) = (\nabla w^h - \boldsymbol{R}_h\boldsymbol{\theta}^h) \\ &= \nabla w^h - [\boldsymbol{J}]^{-\mathrm{T}}\boldsymbol{R}_{\hat{\boldsymbol{A}}}[\boldsymbol{J}]^{\mathrm{T}}\boldsymbol{\theta}^h.\end{aligned}$$

The assumed strain space may be defined as [18]:

$$\begin{aligned}\boldsymbol{\Gamma}_h(A_e) = \big\{\gamma|_{A_e} \in \boldsymbol{S}^h(A_e), [\![\gamma\cdot\boldsymbol{\tau}_i]\!] = 0, \\ \text{on } E_i, \quad i = 1,2,3,4\big\}\end{aligned} \tag{27}$$

with continuous tangential shear strains across element edges. Here E_i are the edges of the quadrilateral element A_e, $\boldsymbol{\tau}_i$ are tangent vectors to the edge E_i, and $[\![\cdot]\!]$ denotes the jump in a quantity across an element interface. $\boldsymbol{S}^h$ is the rectangular rotated Raviart–Thomas space [48],

$$\boldsymbol{S}^h(A_e) = \{\gamma = [\boldsymbol{J}]^{-\mathrm{T}}\hat{\gamma}, \hat{\gamma} \in \boldsymbol{S}^h(\hat{\boldsymbol{A}})\},$$

$$\boldsymbol{S}^h(\hat{\boldsymbol{A}}) = \{\hat{\gamma} = (\gamma_\xi,\gamma_\eta), |\gamma_\xi = a_1 + a_2\eta, \gamma_\eta = b_1 + b_2\xi\}.$$

For completeness, we review the MITC4 strain interpolation.

For the two-dimensional plate element with bilinear mapping (23), covariant basis vectors are defined in terms of the in-plane tangent vectors:

$$\boldsymbol{t}_\xi := \boldsymbol{x}_{,\xi} = [x_{,\xi}, y_{,\xi}]^{\mathrm{T}}, \quad \boldsymbol{t}_\eta := \boldsymbol{x}_{,\eta} = [x_{,\eta}, y_{,\eta}]^{\mathrm{T}}. \tag{28}$$

The complimentary contravariant basis vectors,

$$\boldsymbol{g}^\xi = \frac{1}{J}[y_{,\eta}, -x_{,\eta}]^{\mathrm{T}}, \quad \boldsymbol{g}^\eta = \frac{1}{J}[-y_{,\xi}, x_{,\xi}]^{\mathrm{T}} \tag{29}$$

satisfy the orthogonality conditions, $\boldsymbol{t}_\xi\cdot\boldsymbol{g}^\xi = 1$, $\boldsymbol{t}_\eta\cdot\boldsymbol{g}^\xi = 0$, and $\boldsymbol{t}_\eta\cdot\boldsymbol{g}^\eta = 1$, $\boldsymbol{t}_\xi\cdot\boldsymbol{g}^\eta = 0$, (see [15]). In the above, $J = \det[\boldsymbol{J}] = x_{,\xi}y_{,\eta} - x_{,\eta}y_{,\xi}$, is the element Jacobian. Using this basis, the covariant shear strain tensor components may be written in vector form as [47]:

$$\hat{\gamma} = \hat{\nabla}w - [\boldsymbol{J}]^{\mathrm{T}}\boldsymbol{\theta} = [\boldsymbol{J}]^{\mathrm{T}}(\nabla w - \boldsymbol{\theta}), \tag{30}$$

where

$$\hat{\gamma} = [\gamma_\xi,\gamma_\eta]^{\mathrm{T}}, \quad \hat{\nabla}w = [w_{,\xi}, w_{,\eta}]^{\mathrm{T}}, \quad \boldsymbol{\theta} = [\theta_x,\theta_y]^{\mathrm{T}}. \tag{31}$$

The covariant strains are transformed to cartesian coordinates, using the rotation matrix, $\gamma = [\boldsymbol{J}]^{-\mathrm{T}}\hat{\gamma}$, i.e.,

$$\begin{Bmatrix}\gamma_{xz}\\ \gamma_{yz}\end{Bmatrix} = [\boldsymbol{J}]^{-\mathrm{T}}\begin{Bmatrix}\gamma_\xi\\ \gamma_\eta\end{Bmatrix}, \tag{32}$$

where $\boldsymbol{J}^{-\mathrm{T}}$ is the inverse of $\boldsymbol{J}^{\mathrm{T}}$:

$$[\boldsymbol{J}]^{-\mathrm{T}} = \begin{bmatrix}(\boldsymbol{g}^\xi\cdot\boldsymbol{e}_x) & (\boldsymbol{g}^\eta\cdot\boldsymbol{e}_x)\\ (\boldsymbol{g}^\xi\cdot\boldsymbol{e}_y) & (\boldsymbol{g}^\eta\cdot\boldsymbol{e}_y)\end{bmatrix} = \frac{1}{J}\begin{bmatrix} y_{,\eta} & -y_{,\xi}\\ -x_{,\eta} & x_{,\xi}\end{bmatrix}. \tag{33}$$

Following Bathe and Dvorkin [9], the assumed covariant transverse shear strain field is defined by the linear interpolation between mid-points of the element edges. The essential assumption is to assume the transversal shear interpolation in local convective co-ordinates to be linear in η direction for γ_ξ, and linear in ξ direction for γ_η,

$$\gamma_\xi^h(\eta) = \frac{1}{2}(1-\eta)\gamma_\xi^B + \frac{1}{2}(1+\eta)\gamma_\xi^D, \tag{34}$$

$$\gamma_\eta^h(\xi) = \frac{1}{2}(1-\xi)\gamma_\eta^A + \frac{1}{2}(1+\xi)\gamma_\eta^C. \tag{35}$$

Evaluating the covariant transverse shear strains collocated at the midpoints of the element boundaries, results in the assumed strain field, $\hat{\gamma}^h \in \boldsymbol{S}^h(\hat{\boldsymbol{A}})$,

$$\begin{aligned}\gamma_\xi^h(\eta) = {}&\frac{1}{4}(1-\eta)[(w_2 - w_1) - \boldsymbol{x}_{,\xi}^B\cdot(\boldsymbol{\theta}_2 + \boldsymbol{\theta}_1)] \\ &+ \frac{1}{4}(1+\eta)[(w_3 - w_4) - \boldsymbol{x}_{,\xi}^D\cdot(\boldsymbol{\theta}_3 + \boldsymbol{\theta}_4)],\end{aligned} \tag{36}$$

$$\begin{aligned}\gamma_\eta^h(\xi) = {}&\frac{1}{4}(1-\xi)[(w_4 - w_1) - \boldsymbol{x}_{,\eta}^A\cdot(\boldsymbol{\theta}_4 + \boldsymbol{\theta}_1)] \\ &+ \frac{1}{4}(1+\xi)[(w_3 - w_2) - \boldsymbol{x}_{,\eta}^C\cdot(\boldsymbol{\theta}_3 + \boldsymbol{\theta}_2)],\end{aligned} \tag{37}$$

where

$$\boldsymbol{x}^A_{,\eta} = \boldsymbol{x}^1_{,\eta} = \boldsymbol{x}^4_{,\eta} = (\boldsymbol{x}_4 - \boldsymbol{x}_1)/2,$$
$$\boldsymbol{x}^C_{,\eta} = \boldsymbol{x}^2_{,\eta} = \boldsymbol{x}^3_{,\eta} = (\boldsymbol{x}_3 - \boldsymbol{x}_2)/2,$$
$$\boldsymbol{x}^B_{,\xi} = \boldsymbol{x}^1_{,\xi} = \boldsymbol{x}^2_{,\xi} = (\boldsymbol{x}_2 - \boldsymbol{x}_1)/2,$$
$$\boldsymbol{x}^D_{,\xi} = \boldsymbol{x}^3_{,\xi} = \boldsymbol{x}^4_{,\xi} = (\boldsymbol{x}_3 - \boldsymbol{x}_4)/2.$$

Making use of $N_{i,\xi} = \xi_i(1+\eta_i\eta)/4$, $N_{i,\eta} = \eta_i(1+\xi_i\xi)/4$, it follows that the assumed covariant strain components may also be expressed as

$$\gamma^h_\xi(\eta) = \sum_{i=1}^4 N_{i,\xi} w_i - \sum_{i=1}^4 \overline{N}^i_\xi(\boldsymbol{x}^i_{,\xi}\cdot\boldsymbol{\theta}_i), \tag{38}$$

$$\gamma^h_\eta(\xi) = \sum_{i=1}^4 N_{i,\eta} w_i - \sum_{i=1}^4 \overline{N}^i_\eta(\boldsymbol{x}^i_{,\eta}\cdot\boldsymbol{\theta}_i), \tag{39}$$

where $(\boldsymbol{t}_\xi)_i = \boldsymbol{x}^i_{,\xi}$ and $(\boldsymbol{t}_\eta)_i = \boldsymbol{x}^i_{,\eta}$ are the covariant basis evaluated at the node points, and

$$\overline{N}^1_\eta = \overline{N}^4_\eta = (1-\xi)/4, \quad \overline{N}^2_\eta = \overline{N}^3_\eta = (1+\xi)/4, \tag{40}$$

$$\overline{N}^1_\xi = \overline{N}^2_\xi = (1-\eta)/4, \quad \overline{N}^3_\xi = \overline{N}^4_\xi = (1+\eta)/4. \tag{41}$$

In this form, it is clear that the the assumed covariant strain in natural coordinates may be interpreted as a reduction operation $\boldsymbol{R}_{\hat{A}}$: $[H^1(\hat{A})]^2 \to \boldsymbol{S}^h(\hat{A})$, $\hat{\gamma}^h = \hat{\nabla} w^h - \boldsymbol{R}_{\hat{A}}[\boldsymbol{J}]^{\mathrm{T}}\boldsymbol{\theta}^h$, which interpolates piecewise smooth functions into the space of linear functions, $\hat{\gamma}^h \in \boldsymbol{S}^h(\hat{A})$.

It is this linear strain property that will be used to simplify the residuals R^h_1 and R^h_2 appearing in the F_{LS} functionals given in (17) and (20). In particular, the following important properties of the rotated Raviart–Thomas space for the assumed shear strain interpolation fields are used,

$$\frac{\mathrm{d}}{\mathrm{d}\xi}\left[\gamma^h_\xi(\eta)\right] = 0, \quad \frac{\mathrm{d}}{\mathrm{d}\eta}\left[\gamma^h_\eta(\xi)\right] = 0. \tag{42}$$

Remarks

(i) The form of the MITC4 interpolation for shear strains given here avoids computation of the square-roots appearing in $\|\boldsymbol{x}_{,\xi}\| = (x^2_{,\xi} + y^2_{,\xi})^{1/2}$, $\|\boldsymbol{x}_{,\eta}\| = (x^2_{,\eta} + y^2_{,\eta})^{1/2}$, and used in the original implementation given in [9].

(ii) Following the approach given in Prathap [10], the construction of the finite element space $\boldsymbol{S}^h$ for the assumed strains expressed in (38) and (39), can also be interpreted as a *field consistent* interpolation between $\hat{\nabla} w^h$ and assumed covariant section rotations θ^h_ξ, θ^h_η, interpolated with the smoothing functions given in (40) and (41), i.e.,

$$\theta^h_\xi = \sum_{i=1}^4 \overline{N}^i_\xi(\theta_\xi)_i, \quad \theta^h_\eta = \sum_{i=1}^4 \overline{N}^i_\eta(\theta_\eta)_i. \tag{43}$$

To maintain *edge consistency* (continuous tangential shear strains), the nodal values $(\theta_\xi)_i$ and $(\theta_\eta)_i$ are transformed to Cartesian coordinate definitions of the rotations $(\theta_x)_i$ and $(\theta_y)_i$ using the Jacobian transformation given in (26) evaluated at the nodes,

$$\begin{Bmatrix} (\theta_\xi)_i \\ (\theta_\eta)_i \end{Bmatrix} = [\boldsymbol{J}]_i \begin{Bmatrix} (\theta_x)_i \\ (\theta_y)_i \end{Bmatrix}. \tag{44}$$

Defining the assumed covariant strains by

$$\gamma^h_\xi(\eta) = w^h_{,\xi} - \theta^h_\xi, \quad \gamma^h_\eta(\xi) = w^h_{,\eta} - \theta^h_\eta \tag{45}$$

and using (43) and (44), leads to the expressions given in (38) and (39), or equivalently (36) and (38). In [10], the smoothing functions $\overline{N}^i$ are derived using a least-squares fit of the covariant transverse shear strains within an element. The equivalence between the field and edge consistent development of [10] and the original MITC development of [9] does not seem to be recognized in the open literature, see e.g. [49,50]. The equivalence between different cures for shear locking phenomena is discussed in [25].

4. Evaluating element parameters

In this section, we determine optimal parameters τ_1 and τ_2 appearing in the MLS terms (17) and (20), for the four-node quadrilateral element with assumed transverse shear strain given by the MITC4 mixed interpolation. The dispersion analysis follows the same procedures used in [30] to determine optimal mesh parameters for an assumed stress hybrid least-squares plate element. We begin by simplifying the residuals appearing in the generalized least-squares functionals F_{MLS} and evaluate the repetitive difference stencil associated with a uniform finite element mesh. Using this stencil we obtain the numerical dispersion equation relating wave numbers to real frequency input. Solving this equation gives two root pairs similar to that found for the analytical dispersion relation—one real propagating wave number $\pm k_1$, and one purely imaginary wave number $\pm k_2$. We evaluate the parameters τ_1 and τ_2 by matching the finite element wave number pairs to the analytical wave number pairs for a given free wave angle φ. A similar design criterion for matching the single real valued wave number for the scalar Helmholtz equation in two dimensions was used in [40].

To determine the stencil, we consider a uniform mesh $\mathscr{M}_h$, of four-node quadrilateral elements with element side lengths $h = |\Delta x| = |\Delta y|$. In this mesh we label each node (m,n), where m and n are integers. Thus the coordinates of each node (m,n) are given by $(x_m, y_n) = (mh, nh)$. The nodal degrees-of-freedom at these nodes are denoted $w^h_{m,n} = w^h(x_m, y_n)$, and $\boldsymbol{\theta}^h_{m,n} = \boldsymbol{\theta}^h(x_m, y_n)$.

For a general four-node quadrilateral element characterized by the parametric mapping, $\nabla = [\boldsymbol{J}]^{-\mathrm{T}}\hat{\nabla}$, the Laplacian and divergence operators in natural coordinates may be expressed as

$$\nabla^2 = \frac{1}{J^2}\left(a^2\frac{\partial^2}{\partial\xi^2} + b^2\frac{\partial^2}{\partial\eta^2}\right) - 2\frac{c^2}{J^2}\left(\frac{\partial^2}{\partial\xi\partial\eta} - \boldsymbol{x}_{,\xi\eta}\cdot[\boldsymbol{J}]^{-\mathrm{T}}\hat{\nabla}\right), \tag{46}$$

$$\operatorname{div}\gamma = \frac{1}{J^2}\left(a^2\gamma_{\xi,\xi} + b^2\gamma_{\eta,\eta}\right) - \frac{c^2}{J^2}\left(\gamma_{\xi,\eta} + \gamma_{\eta,\xi} - 2\boldsymbol{x}_{,\xi\eta}\cdot[\boldsymbol{J}]^{-\mathrm{T}}\hat{\gamma}\right), \tag{47}$$

$$\operatorname{div}\boldsymbol{\theta} = \frac{1}{J}\left(\boldsymbol{a}\cdot\boldsymbol{\theta}_{,\xi} + \boldsymbol{b}\cdot\boldsymbol{\theta}_{,\eta}\right), \tag{48}$$

where $\boldsymbol{x}_{,\xi\eta} = \text{constant}$,

$$\boldsymbol{a} = \widehat{\mathbf{curl}}\, y = [y_{,\eta}, -y_{,\xi}]^{\mathrm{T}}, \quad \boldsymbol{b} = -\widehat{\mathbf{curl}}\, x = -[x_{,\eta}, -x_{,\xi}]^{\mathrm{T}} \tag{49}$$

and $a = \|\boldsymbol{a}\|$, $b = \|\boldsymbol{b}\|$, $c^2 = x_{,\xi}y_{,\xi} + x_{,\eta}y_{,\eta}$.

For square element geometries, $x_{,\xi} = y_{,\eta} = h/2$, and $x_{,\eta} = y_{,\xi} = 0$, so that $a^2 = b^2 = h/2$, $c^2 = 0$, and $J = h^2/4$, simplifying the above expressions. The Laplacian reduces to

$$\nabla^2 = \frac{1}{J}\hat{\nabla}^2 = \frac{1}{J}\left(\frac{\partial^2}{\partial\xi^2} + \frac{\partial^2}{\partial\eta^2}\right). \tag{50}$$

From the field-consistent property given in (42) for the rotated Raviart–Thomas space $\hat{\gamma}^h \in \boldsymbol{S}^h(\hat{A})$, the divergence of the MITC4 interpolated shear strains vanishes within the element,

$$\operatorname{div}\gamma^h = \frac{1}{J}\hat{\nabla}\cdot\hat{\gamma}^h = \frac{1}{J}\left(\gamma_{\xi,\xi} + \gamma_{\eta,\eta}\right) = 0, \quad \forall\ \gamma^h \in \boldsymbol{\Gamma}_h. \tag{51}$$

Furthermore, the divergence of the section rotations simplifies to

$$\operatorname{div}\boldsymbol{\theta}^h = \frac{1}{\sqrt{J}}\hat{\nabla}\cdot\boldsymbol{\theta}^h = \frac{1}{\sqrt{J}}\left(\theta^h_{x,\xi} + \theta^h_{y,\eta}\right). \tag{52}$$

Since $\boldsymbol{\theta}^h \in Q^1(\hat{A})$, then $\operatorname{div}\boldsymbol{\theta}^h \in P^1(\hat{A}) = \{\phi|\phi = c_1 + c_2\xi + c_3\eta\}$, and therefore,

$$\nabla^2(\operatorname{div}\boldsymbol{\theta}^h) = \frac{1}{J}\hat{\nabla}^2\left(\frac{1}{\sqrt{J}}\hat{\nabla}\cdot\boldsymbol{\theta}^h\right) = 0, \quad \forall\boldsymbol{\theta}^h \in \boldsymbol{V}^h \tag{53}$$

Using (51) and (53), the residuals in the generalized least-squares functional reduce to,

$$\nabla R^h_1 = \rho t\omega^2\nabla(w^h + f), \quad R^h_2 = \rho I\omega^2\nabla\cdot\boldsymbol{\theta}^h \tag{54}$$

and (17) becomes,

$$F_{\mathrm{LS}} = \frac{1}{2}\sum_{A_e\in\mathscr{M}_h}\int_{A_e}\{r_1\nabla(w^h + f)\cdot\nabla(w^h + f) + r_2(\nabla\cdot\boldsymbol{\theta}^h)^2\}\,\mathrm{d}A, \tag{55}$$

where

$$r_1 = \tau_1\left(\rho t\omega^2\right)^2, \quad r_2 = \tau_2\left(\rho I\omega^2\right)^2, \quad f = q/\left(\rho t\omega^2\right).$$

Similarly, the simplified form (20) reduces for square elements with MITC4 interpolation to,

$$F_{\mathrm{LS}} = \frac{1}{2}\sum_{A_e\in\mathscr{M}_h}\int_{A_e}\left\{r_1\nabla(w^h + f)\cdot\nabla(w^h + f) + r_2\left[(\theta^h_{x,x})^2 + (\theta^h_{y,y})^2\right]\right\}\mathrm{d}A. \tag{56}$$

A similar least-squares stabilizing operator was obtained by the assumed stress hybrid formulation given in [30]. In that case, the simplification arises from the requirement that the assumed stress-field satisfies static equilibrium within A_e.

Substituting the bilinear interpolations for w^h and $\boldsymbol{\theta}^h$, together with the assumed strain γ^h defined by the MITC4 interpolation, into the reduced MLS functionals and imposing stationary conditions with respect to w^h and $\boldsymbol{\theta}^h$, results in the following system of linear algebraic equations for each element,

$$[\boldsymbol{K}^e - \omega^2\boldsymbol{M}^e + r_1(\omega)\hat{\boldsymbol{M}}^e_1 + r_2(\omega)\hat{\boldsymbol{M}}^e_2]\boldsymbol{d}^e = \boldsymbol{f}^e \tag{57}$$

Here, $\boldsymbol{d}^e$ is the 12×1 vector of element nodal displacements derived from $\{\boldsymbol{v}^h(\boldsymbol{x}_i) = (w_i, \boldsymbol{\theta}_i),\ i = 1,\ldots,4\}$, and $\boldsymbol{K}^e$ and $\boldsymbol{M}^e$ are the element stiffness and mass matrices, respectively. The frequency independent stabilization matrices resulting from (55) are defined by

$$\hat{\boldsymbol{M}}^e_1 = \int_{A_e}\left\{\boldsymbol{N}^{\mathrm{T}}_{w,x}\boldsymbol{N}_{w,x} + \boldsymbol{N}^{\mathrm{T}}_{w,y}\boldsymbol{N}_{w,y}\right\}\mathrm{d}A, \tag{58}$$

$$\hat{\boldsymbol{M}}^e_2 = \int_{A_e}\left(\boldsymbol{N}_{\theta_x,x} + \boldsymbol{N}_{\theta_y,y}\right)^{\mathrm{T}}\left(\boldsymbol{N}_{\theta_x,x} + \boldsymbol{N}_{\theta_y,y}\right)\mathrm{d}A, \tag{59}$$

where $\boldsymbol{N}_w$, $\boldsymbol{N}_{\theta_x}$ and $\boldsymbol{N}_{\theta_y}$ are row vectors of bilinear basis functions defined by the interpolations (25) written in vector form,

$$w^h = \boldsymbol{N}_w\boldsymbol{d}^e, \quad \theta^h_x = \boldsymbol{N}_{\theta_x}\boldsymbol{d}^e, \quad \theta^h_y = \boldsymbol{N}_{\theta_y}\boldsymbol{d}^e. \tag{60}$$

Here, we have assumed r_i, $i = 1,2$ are constant within A_e, although variable r_i are possible. Alternatively, the simplified form resulting from (56) may be used, with the modified matrix,

$$\widetilde{\boldsymbol{M}}^e_2 = \int_{A_e}\left\{\boldsymbol{N}^{\mathrm{T}}_{\theta_x,x}\boldsymbol{N}_{\theta_x,x} + \boldsymbol{N}^{\mathrm{T}}_{\theta_y,y}\boldsymbol{N}_{\theta_y,y}\right\}\mathrm{d}A. \tag{61}$$

For square elements, the stabilization matrix for the simplified form,

$$\widetilde{\boldsymbol{M}}^e(\omega) = r_1(\omega)\hat{\boldsymbol{M}}_1^e + r_2(\omega)\widetilde{\boldsymbol{M}}_2^e \tag{62}$$

can be written in nodal block form as

$$\widetilde{\boldsymbol{M}}^e = \frac{1}{6}\begin{bmatrix} \boldsymbol{A} & \boldsymbol{B} & \boldsymbol{C} & \boldsymbol{D} \\ \boldsymbol{B} & \boldsymbol{A} & \boldsymbol{D} & \boldsymbol{C} \\ \boldsymbol{C} & \boldsymbol{D} & \boldsymbol{A} & \boldsymbol{B} \\ \boldsymbol{D} & \boldsymbol{C} & \boldsymbol{B} & \boldsymbol{A} \end{bmatrix} \tag{63}$$

with diagonal nodal blocks,

$$\boldsymbol{A} = \mathrm{diag}(4r_1, 2r_2, 2r_2), \quad \boldsymbol{C} = \mathrm{diag}(-2r_1, -r_2, -r_2),$$
$$\boldsymbol{B} = \mathrm{diag}(-r_1, -2r_2, r_2), \quad \boldsymbol{D} = \mathrm{diag}(-r_1, r_2, -2r_2).$$

A similar closed form expression can be obtained using (59).

Finite element difference relations associated with a typical node location (x_m, y_n) are obtained by assembling a patch of four elements. The result is a coupled system of three, 27-term difference stencils associated with the three nodal degrees-of-freedom and nine connected nodes centered at node (m,n). Let E_x^p and E_y^q be defined by the directional shift operations:

$$E_x^p \boldsymbol{d}_{(m,n)} := \boldsymbol{d}_{(m+p,n)}, \quad E_y^q \boldsymbol{d}_{(m,n)} := \boldsymbol{d}_{(m,n+q)}. \tag{64}$$

Then the stencil associated with the solution $\boldsymbol{d}_{(m,n)} = \boldsymbol{v}^h(x_m, y_n)$, may be expressed in the form,

$$\sum_{p=-1}^{1}\sum_{q=-1}^{1}[\boldsymbol{D}_{pq}]E_x^p E_y^q \boldsymbol{d}_{(m,n)} = \{\boldsymbol{0}\}, \tag{65}$$

where $[\boldsymbol{D}_{pq}]$ are 3×3 nodal partitions defined by the nine-point block difference star associated with the nine connected nodes.

4.1. Finite element dispersion relation

To obtain the finite element dispersion relation associated with this stencil, a plane wave solution is assumed for the nodal displacements, similar in form to the analytical solution to the homogeneous problem:

$$\boldsymbol{d}_{(m,n)} = \begin{Bmatrix} w_0 \\ \theta_0 \boldsymbol{v} \end{Bmatrix} \mathrm{e}^{(\mathrm{i}k_x^h hm)} \mathrm{e}^{(\mathrm{i}k_y^h hn)}, \tag{66}$$

where $k_x^h = k^h \cos\varphi$, $k_y^h = k^h \sin\varphi$ are components of the wave vector $\boldsymbol{k}^h = k^h \boldsymbol{v} = k^h(\cos\varphi, \sin\varphi)$. Substitution of (66) into the stencil equations (65), leads to the finite element dispersion relation for the plate expressed as

$$\mathscr{D}(k^h, \omega) := \hat{G}_{11}\hat{G}_{22} - \hat{G}_{12}^2 = 0. \tag{67}$$

For the MLS4 element, the frequency dependent coefficients take the form,

$$\hat{G}_{11} = G_{11} + r_1 H_{11}, \quad \hat{G}_{22} = G_{22} + r_2 \hat{H}_{22}, \quad \hat{G}_{12} = G_{12}. \tag{68}$$

The functions G_{11}, G_{22} and G_{12} depend on the stiffness and mass matrix coefficients K_{ij}^e and M_{ij}^e, the frequency ω, wave number k^h, and wave angle φ. The form of these functions are defined in [30], with the stiffness and mass matrices replaced with those arising from the MITC4 interpolation.The functions resulting from the least-squares stabilization matrices (58) and (59) are defined by,

$$H_{11} = (4 - c_x - c_y - 2c_x c_y)/2,$$
$$\hat{H}_{22} = a_1 + a_2/2 + 3a_3/4.$$

$$a_1 = 1 - c_x \cos^2\varphi - c_y \sin^2\varphi,$$
$$a_2 = c_y \cos^2\varphi + c_x \sin^2\varphi - c_x c_y,$$
$$a_3 = s_x s_y \sin 2\varphi.$$

$$c_x = \cos\left(k^h h\cos\varphi\right), \quad c_y = \cos\left(k^h h\sin\varphi\right),$$
$$s_x = \sin\left(k^h h\cos\varphi\right), \quad s_y = \sin\left(k^h h\sin\varphi\right). \tag{69}$$

For the simplified least-squares stabilization matrix defined in (62), $\hat{H}_{22}$, reduces to $\hat{H}_{22} = a_1 + a_2/2$. This simplified coefficient is identical to that found in the hybrid least-squares (HLS4) element in [30]. This result follows from the fact that both MLS4 and HLS4 use bilinear interpolation of section rotations $\boldsymbol{\theta}^h$ with simplified matrix in the form (62). Additional functions related to the mesh parameter r_1 are present in the HLS4 element due to the cross-coupling of the nodal deflections and section rotations in the vertical displacement approximation.

The finite element dispersion equation $\mathscr{D}(\omega, k^h h, \varphi, K_{ij}, M_{ij}, r_1, r_2)$ defined in (67) relates frequency ω, to the numerical wave number $k^h h$ and φ, and depends on the stiffness and mass coefficients $K_{ij} = [\boldsymbol{K}^e]_{ij}$, and $M_{ij} = [\boldsymbol{M}^e]_{ij}$, and mesh parameters r_1, r_2. Similar to the analytic dispersion relation, there are two pairs of numeric wave numbers $\pm k_1^h$ and $\pm k_2^h$ that satisfy (67) which correspond to propagating and evanescent waves, respectively. For waves directed along mesh lines corresponding to $\varphi = 0$, then, $a_3 = 0$, so that $\hat{H}_{22} = 1 - c_x + (c_y - c_x c_y)/2$, and as expected the dispersion relation for both MLS4-1 and MLS4-2 are the same.

4.2. Selection of optimal design parameters

Following the procedures employed in [30], mesh parameters r_1 and r_2 are determined such that the finite element wave number pairs match the analytical wave number pairs $\pm k_1$ and $\pm k_2$ for a given orientation $\varphi = \varphi_0$. In particular, we set $k^h = k_1(\omega)$ and $k^h = k_2(\omega)$ in the finite element dispersion relation (67). In particular, we replace $(k^h h\cos\varphi, k^h h\sin\varphi)$, in (69) with $(k_1 h\cos\varphi, k_1 h\sin\varphi)$, and $(k_2 h\cos\varphi, k_2 h\sin\varphi)$, respectively. This results in two equations for r_1 and r_2:

$$c_{11} + c_{12}r_1 + c_{13}r_2 + c_{14}r_1r_2 = 0, \tag{70}$$

$$c_{21} + c_{22}r_1 + c_{23}r_2 + c_{24}r_1r_2 = 0, \tag{71}$$

with coefficients $c_{1i} = c_i(k_1, \varphi)$, and $c_{2i} = c_i(k_2, \varphi)$, $i = 1$, 2, 3, 4, defined by substituting k_1 and k_2 into the functions,

$$\begin{aligned} c_1 &= G_{11}G_{22} - G_{12}G_{12}, \\ c_2 &= G_{22}H_{11}, \\ c_3 &= G_{11}\hat{H}_{22}, \\ c_4 &= H_{11}\hat{H}_{22}. \end{aligned}$$

Eliminating r_2 from (70) and (71), allows the design parameter r_1 to be obtained in closed-form by solving the *quadratic* equation

$$e_2r_1^2 + e_1r_1 + e_0 = 0, \tag{72}$$

where $e_l = e_l(c_{ij})$, $l = 0$, 1, 2, are defined by,

$$\begin{aligned} e_2 &= c_{24}c_{12} - c_{14}c_{22}, \\ e_1 &= c_{23}c_{12} - c_{13}c_{22} + c_{11}c_{24} - c_{21}c_{14}, \\ e_0 &= c_{11}c_{23} - c_{21}c_{13}. \end{aligned}$$

For the MLS4 element, solution of the quadratic equation (72) results in two real negative roots. We select the largest root to determine r_1, as this root matches the analytical dispersion relations. The other design parameter can then be written in terms of the first,

$$r_2 = -\frac{c_{21}r_1 + c_{11}}{c_{31} + c_{41}r_1}. \tag{73}$$

Remark. For the HLS4 element derived in [30], a *cubic* equation in r_1 results from cross-coupling of section rotations in the deflection approximation, thus requiring more work to compute roots.

The design parameters $r_l = r_l(K_{ij}, M_{ij}, \omega, h, \varphi)$, $l = 1, 2$ are obtained in terms of the stiffness and mass coefficients in the underlying MITC4 element, the frequency dependent wave numbers satisfying the analytical dispersion relation, and φ. In general, the direction of wave propagation φ is not known a priori. However, similar to [40,30], we can select an angle in the definitions for r_1 and r_2 which minimizes dispersion error over the periodic interval $0 \leqslant \varphi \leqslant \pi/4$. With the choice $\varphi = 0°$ in the definitions for r_1 and r_2, then, as expected, the dispersion relations for our MLS4 plate element specialize to the relations for the GGLS 1-D Timoshenko beam element described in [45], with $EI = Et^3/12(1 - \nu^2)$.

4.3. Distorted elements

For distorted quadrilateral finite element geometries, the simplifications indicated in (54) are no longer strictly valid. For the MITC4 interpolations on distorted bilinear quadrilateral elements, the divergence of the assumed strain $\gamma^h \in \boldsymbol{\Gamma}^h(A_e)$ and Laplacian operator acting on the divergence of the section rotations $\boldsymbol{\theta}^h$, are not necessarily zero. In this case, and with the MITC4 interpolation $\hat{\gamma}^h \in \boldsymbol{S}^h(\hat{A})$, the gradient of the shear residual within an element takes the form,

$$\nabla R_1^h = [\boldsymbol{J}]^{-\mathrm{T}}\hat{\nabla}\Big[\rho t\omega^2\big(w^h + f\big) - \frac{c^2}{J^2}\Big(\gamma^h_{\xi,\eta} + \gamma^h_{\eta,\xi} - 2\boldsymbol{x}_{,\xi\eta}\cdot[\boldsymbol{J}]^{-\mathrm{T}}\hat{\gamma}^h\Big)\Big], \tag{74}$$

where $\gamma^h_{\xi,\eta} = \text{constant}$, $\gamma^h_{\eta,\xi} = \text{constant}$. However, in implementing our MLS method on nonuniform meshes, we neglect the effect of the relatively small mixed derivatives and Laplacian on the residuals, and revert to (54). Thus for distorted elements, we retain the form of the stabilization matrices (58) and (59), with constant element jacobian $[\boldsymbol{J}] = (h_e^2)\boldsymbol{I}$, consistent with the mesh parameter definitions for r_1 and r_2. We define the element length h_e by either a local size determined by the square root of the element area, $h_e = \sqrt{A_e}$, or by an average element length h_{ave} computed over a patch of similarly sized elements. While our definition for the mesh parameters r_1 and r_2 were derived from a dispersion relation on a uniform mesh, with constant element length h_e, accurate solutions on nonuniform meshes are shown to be relatively insensitive to the precise definitions used.

5. Dispersion accuracy

For a range of frequencies ω, and wave angles φ, relative to uniform mesh lines, the wave number accuracy for our residual-based MLS4 four-node element is compared with the underlying MITC4 element [9], and the SRI4 element [7]. Results are presented for a steel plate with properties: $E = 210 \times 10^{10}$ dynes/cm^2, $\nu = 0.29$, $\rho = 7.8$ g/cm^2, plate thickness $t = 0.15$ cm, and shear correction factor $\kappa = 5/6$. The node spacing is $h = \Delta x = \Delta y = 1.0$ cm, resulting in a ratio of plate thickness to element length of $t/h = 3/20$. Both dispersion analysis and numerical examples show similar solutions using the original divergence form F_{LS} defined in (55) and the simplified form defined in (56). For this reason, results for our four-node quadrilateral element MLS4 are reported for the simplified residual-based form (56).

We begin with a dispersion analysis of the underlying MITC4 element. The resulting numerical wave numbers k_1^h and k_2^h for the MITC4 element are compared to the analytical wave number–frequency relation in Fig. 1. We note that the dispersion curves for the MITC4 element for uniform meshes are nearly identical to the results for the SRI4 element, see [29,30]. In the frequency range plotted, both the analytical and numerical wave number exhibit one real wave number k_1, corresponding to a

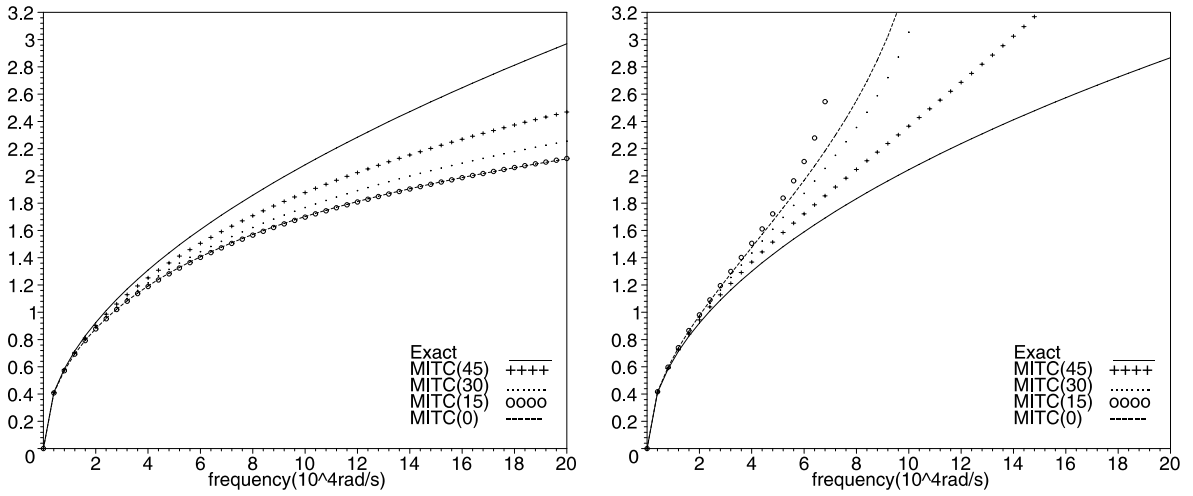

Fig. 1. Dispersion curves relating wave number to frequency ω, at wave angles $\varphi = 0°, 15°, 30°, 45°$. Comparison with MITC4 (φ) and exact. Left: real propagating wave number k_1, Right: imaginary evanescent wave number k_2.

propagating wave, and one purely imaginary wave number k_2, corresponding to an evanescent decaying wave. Results are plotted for equally spaced angles $\varphi = 0°, 15°, 30°, 45°$. Due to symmetry, results are bounded by the extreme angles of 0° and 45°, corresponding to waves directed along mesh lines and mesh diagonals, respectively. The values are plotted over the range $0 < kh < \pi$. The upper limit with real numerical wave number $k_1^h h = \pi$ corresponds to two elements per wavelength. Beyond this value, the real numerical wave numbers become complex, resulting in the spurious behavior of rapid amplitude decay. The frequency associated with this limiting wave number is called the 'cut-off' frequency associated with the discrete mesh.

To quantify the dispersion error, the relative error of the numerical wave number divided by the analytic wave number, k^h/k is shown in Fig. 2. The frequency is plotted over the range up to $\omega h = 5 \times 10^4$ cm/s corresponding to the more practical limit of approximately four elements per wavelength. At low frequencies, the MITC4 element replicates the character of the analytic dispersion curves marginally well with error in the real propagating wave number <3% for discretizations finer than 10 elements per wavelength, i.e., $10h = \lambda$. Recall wavelength is defined as $\lambda = 2\pi/k$, so that 10 elements/wavelength corresponds to $kh = \pi/5 \approx 0.63$, and $\omega h \approx 1 \times 10^4$ cm/s. Above this level, the error in both the real and imaginary wave number increases rapidly. We note that at 10 elements per wavelength, the error in the propagating plate wave number is nearly double the 1.6% dispersion error exhibited by the Galerkin finite element discretization for the scalar Helmholtz equation [52,40]. To achieve the same 1.6% level of accuracy would require more than 20 MITC4 plate elements per wavelength. This observation shows the relatively poor accuracy of the MITC4 plate elements and provides strong motivation for designing modified Mindlin plate elements with improved phase accuracy. Starting from waves directed along mesh lines at $\varphi = 0°$, the dispersion error for the MITC4 element increases slightly for waves approaching an angle of $\varphi = 15°$, and then decreases after that. The error is smallest for waves directed at $\varphi = 45°$ along mesh diagonals. A minimum phase error at $\varphi = 45°$ is also observed in the behavior of the Galerkin finite element discretization of the scalar Helmholtz equation [40].

The bottom two plots in Fig. 2 show the improved dispersion accuracy achieved for both the real and imaginary wave numbers by the residual-based MLS4 element with r_1 and r_2 defined with $\varphi = 30°$. The MLS4 method exactly matches the analytic wave numbers at $\varphi = 30°$, over all frequencies, as required by our definition of the mesh parameters. For other wave angles, the MLS4 element replicates the character of the analytical dispersion curves well with significant reduction in numerical wave number error compared to the underlying MITC4 interpolation. For the MLS4 modification, the error is bounded above and below the exact value at $\varphi = 30°$. Results for the MLS4 method give a maximum error in the real wave number <1% at a frequency of $\omega h = 1 \times 10^4$ cm/s, corresponding to approximately 10 elements per wavelength. This represents a nearly threefold reduction in phase error compared to the base MITC4 element. At the level of 10 elements per wavelength, the maximum error in the imaginary wave number is reduced from 3% for MITC4 to <2% for MLS4. Above this level, the MLS4 shows significant reduction in the imaginary wave number error, indicat-

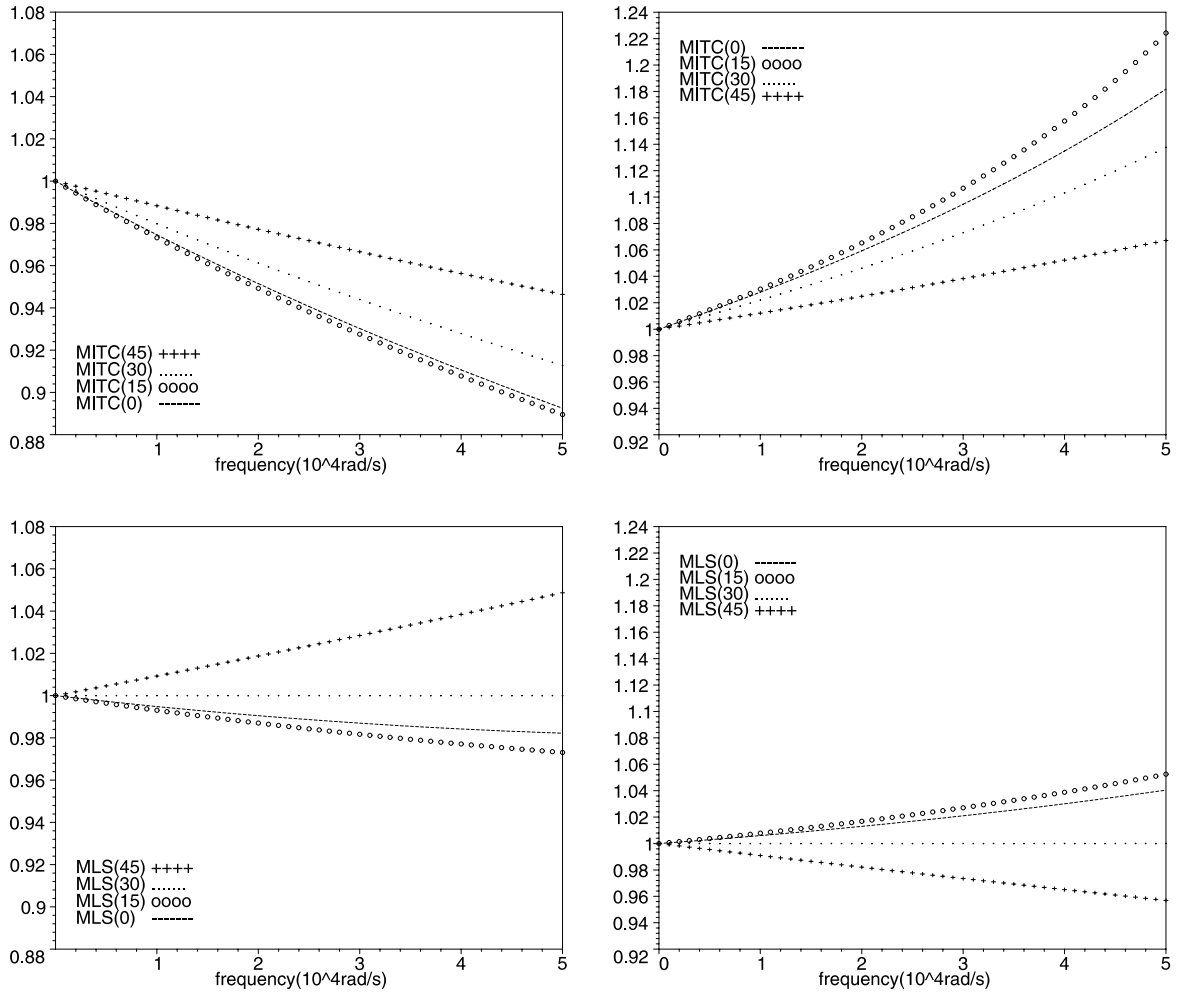

Fig. 2. Relative error k^h/k at angles $\varphi = 0°$, 15°, 30°, 45°. Top: MITC4, Bottom: MLS4 with $\varphi = 30°$ in definition of mesh parameters r_1 and r_2. Left: real wave number k_1, Right: imaginary wave number k_2.

ing improved accuracy for decaying waves near point drivers and discontinuities. As shown in the numerical examples to follow, the real wave number component corresponding to propagating waves, often plays a key role in time-harmonic forced vibration, e.g. for common plate structures with relatively wide spacing between discontinuities. Thus by reducing the percent error in the real wave number, even if by only a small amount, the overall accuracy of the numerical solution can increase significantly. Reduced real wave number (phase) error also minimizes pollution effects exhibited at high frequencies and near eigenfrequencies [43]. Pollution errors are associated with finite element approximations of distributed loads and force resultant (natural) boundary conditions which are not accounted for in the dispersion analysis of an infinite uniform mesh.

For comparison, Fig. 3 shows the relative error k^h/k for the MLS4 element designed to match the analytical wave numbers at the extreme angles of $\varphi = 0°$ and $\varphi = 45°$, i.e., with $\varphi = 0°$ and $\varphi = 45°$ in the definition of r_1 and r_2. With these mesh parameters the wave number accuracy is also improved over all angles compared to the underlying MITC4 element. However, the choice $\varphi = 30°$ in the definitions for r_1 and r_2 gives the best overall dispersion accuracy over the entire range of possible angles defined by the periodic interval $0 \leqslant \varphi \leqslant \pi/4$.

Fig. 4 shows a comparison of the two alternative MLS4-1 and MLS4-2 elements, defined by the stabilization matrices (58), combined with (59) or (61); both with mesh parameters r_1 and r_2 designed to match the analytic wave numbers at $\varphi = 30°$. Error results are shown at the extreme angles $\varphi = 0°$ and $\varphi = 45°$. Due to the small influence of the mixed derivatives in (59), the accuracy is shown to be nearly identical for the alternative MLS4-1 and MLS4-2 formulations.

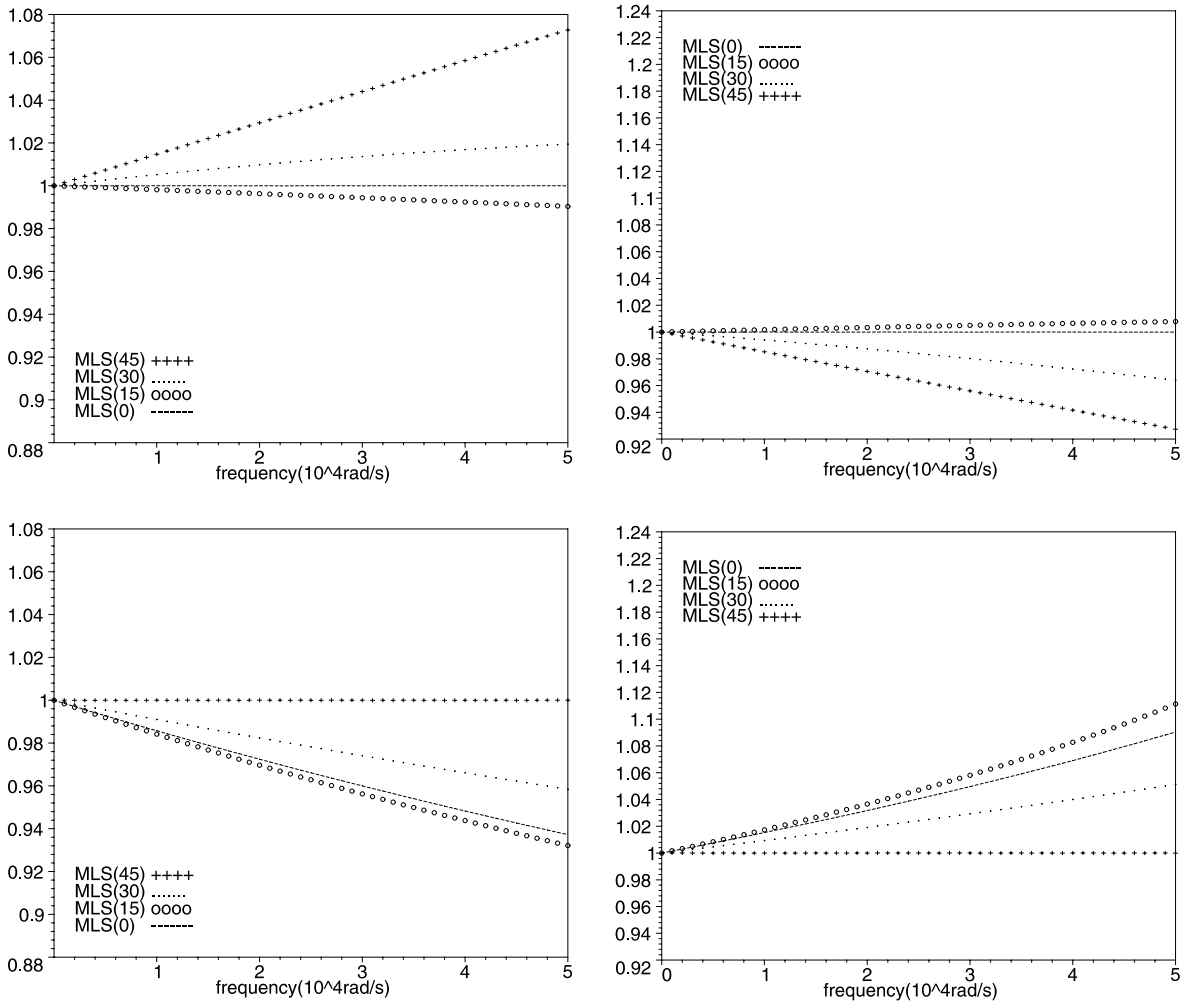

Fig. 3. Relative error k^h/k at angles $\varphi = 0°$, 15°, 30°, 45°. Top: MLS4 with $\varphi = 0°$ in definition of mesh parameters r_1 and r_2. Bottom: MLS4 with $\varphi = 45°$ in definition of mesh parameters r_1 and r_2. Left: real wave number k_1, Right: imaginary wave number k_2.

The frequency and wave angle dependence of the parameters r_1 and r_2 is shown in Fig. 5. In the static limit $\omega \to 0$, $r_1 \to 0$, and $r_2 \to 0$; as a result, the dynamic coefficient matrix tends to the frequency independent stiffness matrix, i.e., the MLS4 element inherits the static behavior of the underlying MITC4 element. This result is the key feature in successfully designing improved residual based methods for time-harmonic response of mixed Mindlin plate elements with arbitrary quadrilateral shape which are free-from shear locking and spurious modes.

6. Numerical examples

6.1. Simply supported plate with uniform loading

Results are presented for forced vibration of a simply supported steel plate with a uniformly distributed time-harmonic pressure loading $q = 2$ dynes/cm^2. We use the same material properties used in the dispersion analysis discussed in the proceeding section. The plate is square with side length $L = 100$ cm. The origin of a Cartesian coordinate system is positioned at the lower left corner of the plate. Using symmetry, only the upper-right $1/4$ of the square is modeled. The finite element solution for the total plate is obtained from a reflection about the lines of symmetry. Results are compared for the different quadrilateral plate elements and the analytical series solution based on the superposition of mode shapes for the Reissner–Mindlin plate model given in [3,30]. For reference, contours of the analytical solution in the upper-right quadrant are shown in Fig. 6 for frequencies $f = 500$ and 1671 Hz.

6.1.1. Uniform meshes

We begin with a numerical study of solutions on a uniform mesh of $N \times N$ elements. In Fig. 7, the vertical

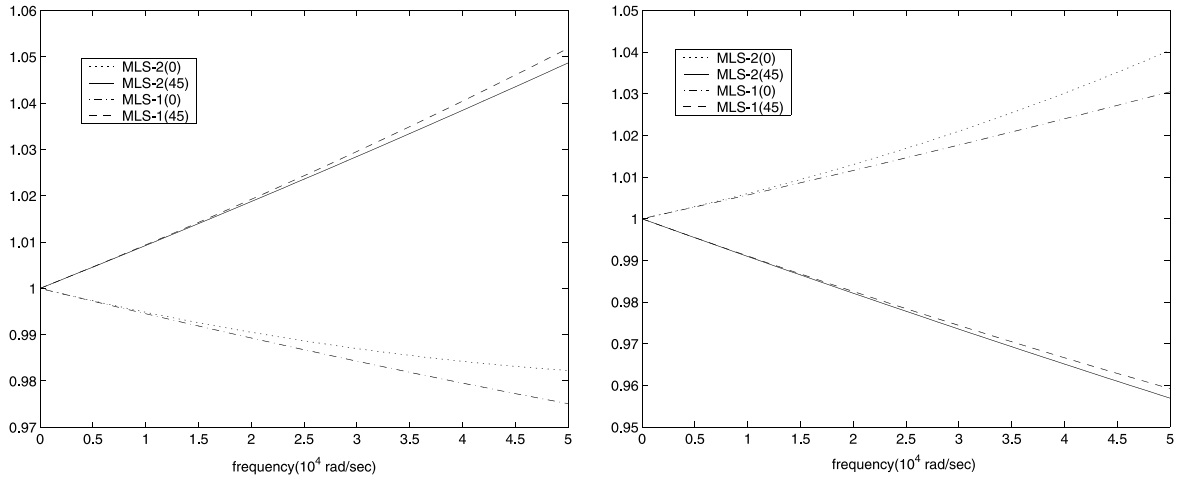

Fig. 4. Relative error k^h/k for the MLS4 element with $\varphi = 30°$ in the definition of mesh parameters r_1, r_2, at bounding angles $\varphi = 0°$, 45°. Comparison between use of stabilization matrix (58) combined with (59), denoted MLS4-1, and simpified form (61), denoted MLS4-2. Left: real wave number k_1, Right: imaginary wave number k_2.

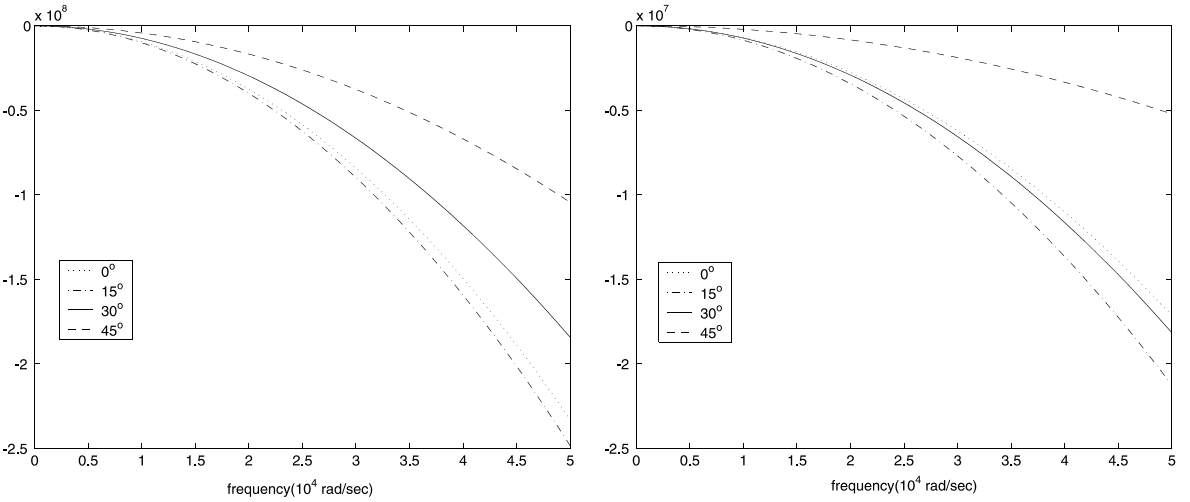

Fig. 5. Frequency dependence on mesh parameters $r_1(\omega, \varphi)$ and $r_2(\omega, \varphi)$ defined by different angles φ. Left: r_1, Right: r_2.

deflection $w^h(x, y)$ is plotted along a horizontal mesh line at a representative cut at $y = 72$ cm. The driving frequency of $f = 500$ Hz, ($\omega = 0.314 \times 10^4$ rad/s) falls between the resonance eigenfrequencies of 450 and 625 Hz. The top figure shows the solution profile using a uniform 50×50 element mesh over $1/4$ of the plate, resulting in an element size $h = 1.0$. At this frequency and mesh size the plate is modeled with approximately 18 elements per wavelength. At this level of discretization, the MITC4 element solution shows large errors while the MLS4 element solution shows good agreement with the analytical solution. As the number of elements is increased to a uniform 100×100 mesh over a quadrant, corresponding to an element size $h = 0.5$ cm, and a discretization of approximately 35 elements per wavelength, both elements match the analytical solution well, although there is still some error shown in the MITC4 solution. These results primarily demonstrate the impact of the phase error in the real wave number as seen in the finite element dispersion relations.

The accuracy is quantified further by computing the relative discrete L_2 error in the vertical deflection measured over the entire plate:

$$\frac{\|e\|_{L_2}}{\|w\|_{L_2}} = \frac{\sqrt{\sum_n \left[w^h(x_n, y_n) - w(x_n, y_n)\right]^2}}{\sqrt{\sum_n \left[w(x_n, y_n)\right]^2}}. \tag{75}$$

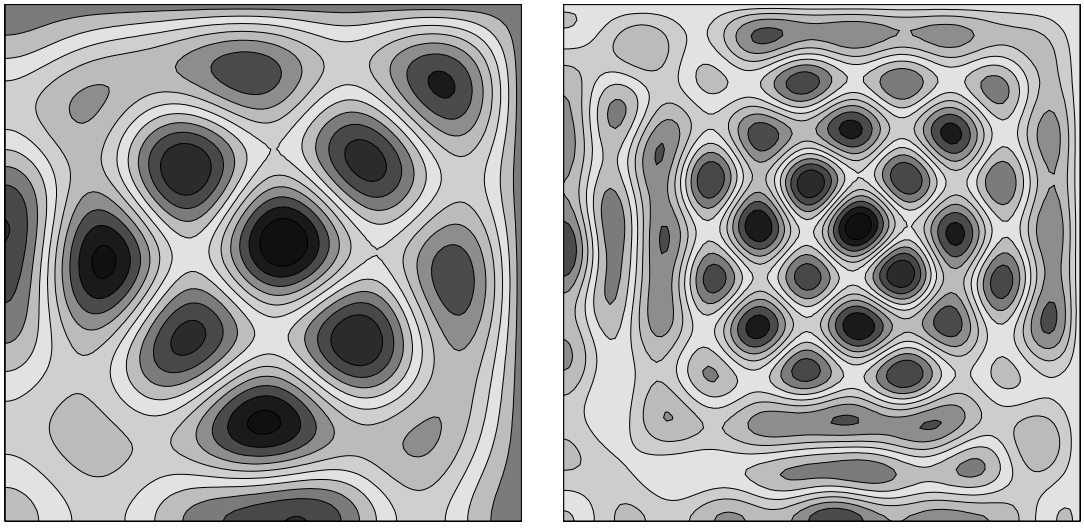

Fig. 6. Contour plot of analytical series solution for vertical deflection in the upper-right quadrant of a simply supported Reissner–Mindlin plate with uniform pressure load, at frequency. Left: $f = 500$ Hz, Right: $f = 1671$ Hz.

In the above, $w^h(x_n, y_n)$ is the finite element solution at a node point with coordinates x_n, y_n, and $w(x_n, y_n)$ is the analytical solution evaluated at the same node point. Fig. 8 shows the L_2 convergence rates with uniform mesh refinement. Both MITC4 and MLS4 achieve the same rate of convergence at approximately $N = 100$ elements. However, as a result of improved dispersion accuracy, the MLS4 element decreases the L_2 error for the same number of elements.

Fig. 9 shows the solution profile when the frequency is increased to $f = 1750$ Hz. This frequency falls between eigenfrequencies at 1627 and 1950 Hz. With a relatively course mesh ($h = 0.5$ cm), the MLS4 solution captures the behavior of the analytical solution well, while the MITC4 solution shows large errors. Using a finer mesh of $h = 0.25$, the MLS4 solution matches the analytical solution, while the MITC4 solution still has not fully converged. Fig. 10 shows the solution profile when the frequency is decreased to $f = 1671$ Hz, ($\omega = 1.05 \times 10^4$ rad/s). This frequency falls relatively close to an eigenfrequency at $f_i = 1627$ Hz, representing a more difficult problem near an ill-conditioned solution (resonance). With element element size $h = 0.5$, the error in the MITC4 element solution is severe, resulting in a complete misrepresentation of the analytical solution. In contrast, the solution for MLS4 follows closely the behavior of the analytical solution. As the mesh is decreased to $h = 0.25$, the MLS4 matches the analytical solution well, while the MITC4 element still shows relatively large errors. The difficulty in resolving the solution near eigenfrequencies can be explained by the pollution effect for the indefinite system under consideration; see [43] for a discussion of this effect for the wave response of the related scalar Helmholtz equation. We see significant increase of the pollution effect when the frequency is moved towards an eigenfrequency. The mesh must be relatively fine in order to achieve a reliable resolution of the resonance behavior (dynamic instability). However, the MLS4 element reduces the pollution effect significantly compared to the underlying MITC4 element.

6.1.2. Quasi-uniform meshes

We next study the performance of the MLS4 element for quasi-uniform meshes (parametric mesh grading). Here, the MLS4 element is computed with mesh parameters r_1 and r_2 determined from an average element size h_{ave}, computed over the total mesh, denoted MLS4-ave, and from a local element size $h_e = \sqrt{A_e}$, denoted MLS4-local. Table 1 shows results obtained using the three different quasi-uniform meshes shown in Fig. 11. We observe that the large improvement in accuracy using the MLS4 element compared to the MITC4 element for uniform meshes is not drastically affected by the element distortions or higher aspect ratios. Showing the robustness of the MLS method, the discrete L_2 error for the MLS4-local solution remains an order of magnitude lower than the underlying MITC4 element for all three quasi-uniform meshes. The MLS4-ave solution, with an average element size over the entire mesh, defined by $h_{\text{ave}} = \sqrt{A/N_{\text{T}}}$, where A is the area and $N_{\text{T}} = 50 \times 50$ is the total number of elements, also reduces the error significantly compared to the MITC4 element. For the quasi-uniform meshes studied, the local mesh size parameter gives better accuracy than the global average.

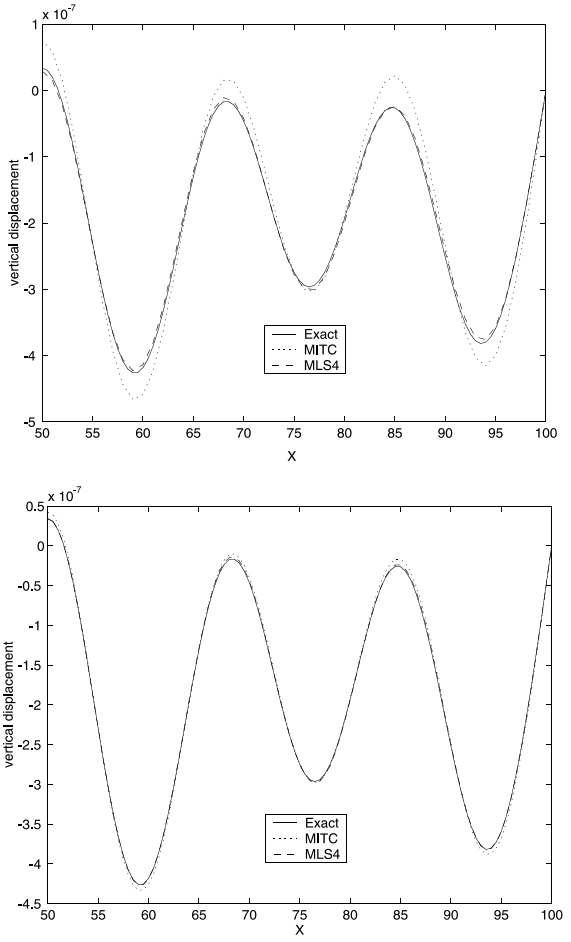

Fig. 7. Simply supported steel plate with uniform distributed time-harmonic loading. Vertical deflection at $y = 72$ cm, $50 \leqslant x \leqslant 100$ cm, frequency $f = 500$ Hz. Uniform mesh with element length, Top: $h = 1.0$ cm, Bottom: $h = 0.5$ cm.

We next study the effect of random mesh distortion on the accuracy of the MLS4 plate element. The distorted mesh is based on the uniform $N \times N$ mesh of equal squares, where each node is allowed to move randomly within a fixed range defined by a 'blur' function Δ, defined as a fraction of the baseline square mesh length h. The nodal coordinates are allowed to vary within the range defined by $(x, y) = (x_m, y_n) + (\epsilon_1, \epsilon_2)\Delta$, where the parameters ϵ_1, and ϵ_2 are random numbers defined in the range $-1 \leqslant \epsilon \leqslant 1$. A value of $\Delta = 0$ corresponds to a uniform mesh. As Δ increases, the elements are further distorted. Tables 2 and 3 show comparisons of relative discrete L_2 error with the blur function ranging from $0 \leqslant \Delta \leqslant 0.4h$. Results are compared at a frequency $f = 500$ Hz, and mesh sizes $h = 1.0$ and 0.5 cm, respectively. For the uniform mesh ($\Delta = 0$) results for SRI4 and MITC4 are nearly identical. The error is reduced significantly for the MLS4 element. For

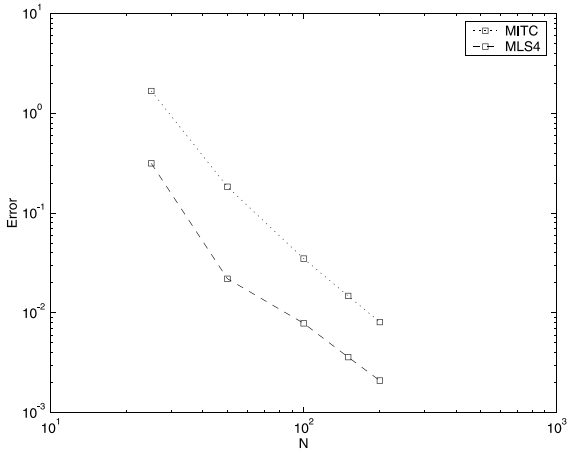

Fig. 8. Simply supported steel plate example. Frequency $f = 500$ Hz. Convergence with mesh refinement. Relative discrete L_2 error for a uniform mesh of $N \times N$ elements over one-quarter of the plate.

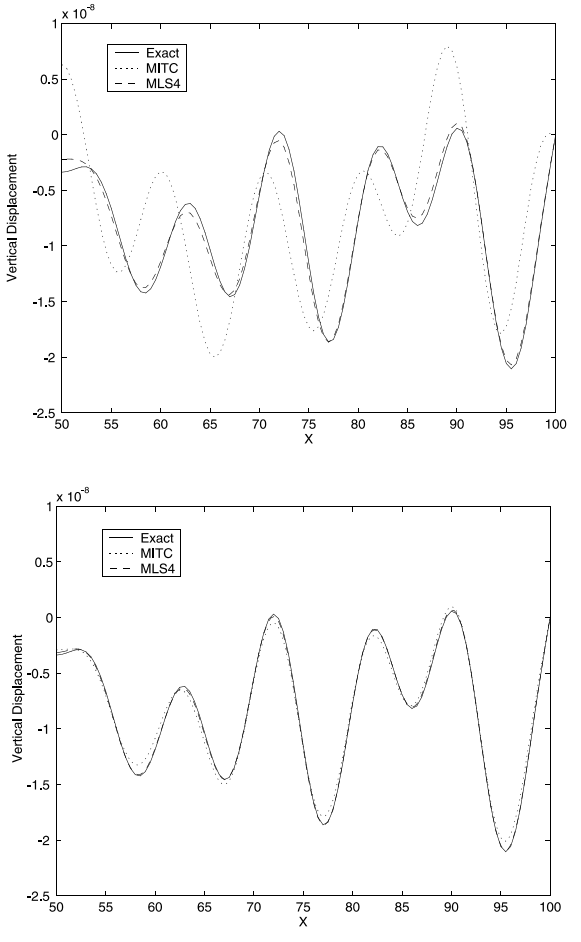

Fig. 9. Simply supported steel plate example. Vertical deflection at $y = 72$ cm, $50 \leqslant x \leqslant 100$ cm, frequency $f = 1750$ Hz. Uniform mesh with element length, Top: $h = 0.5$ cm, Bottom: $h = 0.25$ cm.

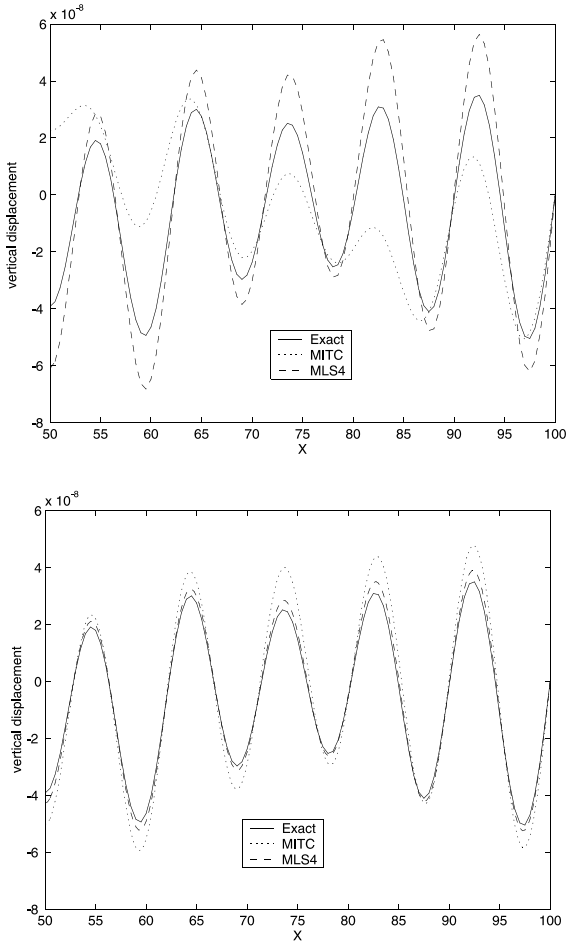

Fig. 10. Simply supported steel plate example. Vertical deflection at $y = 72$ cm, $50 \leqslant x \leqslant 100$ cm, frequency $f = 1671$ Hz. Uniform mesh with element length; Top: $h = 0.5$ cm, Bottom: $h = 0.25$ cm.

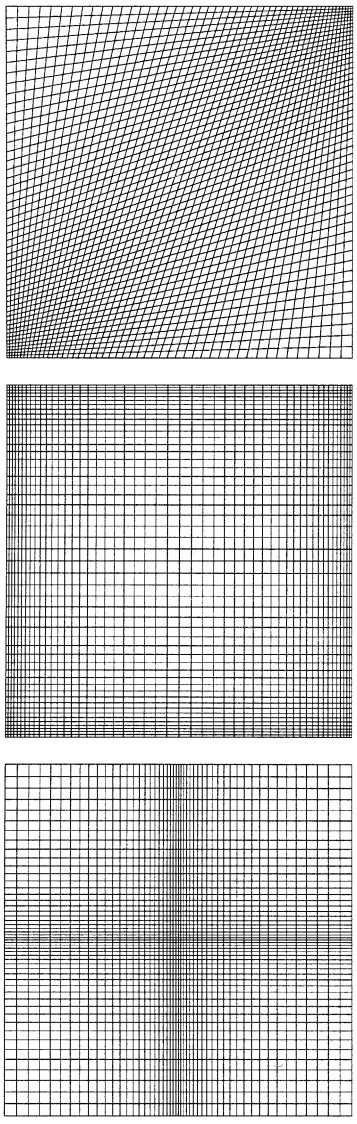

Fig. 11. Quasi-uniform meshes with $N = 50$ elements per edge and 5:1 bias. Average element size $h_{\text{ave}} = \sqrt{A/N_{\text{T}}} = 1.0$. Top: QMesh1, Middle: QMesh2, Bottom: QMesh3.

the MITC4 and MLS4 solutions the error increases somewhat with the first level of distortion $\Delta = 0.1h$, but then is relatively insensitive to further element distortion. For the SRI4 solution, however, the accuracy is decreased significantly with mesh distortion. The distortion seriously affects the accuracy of the SRI element, yet has little significant influence on the error for the MITC4 and MLS4 elements. The results clearly show

Table 1
Discrete L_2 error for square plate example with quasi-uniform meshes at $f = 500$ Hz

Mesh	Element type			
	SRI4	MITC4	MLS4-ave	MLS4-local
QMesh1	0.29952E0	0.29952E0	0.55688E−1	0.38146E−1
QMesh2	0.38511E0	0.38514E0	0.12876E0	0.52325E−1
QMesh3	0.33728E0	0.33731E0	0.32663E−1	0.33728E−1
Uniform	0.18351E0	0.18352E0	0.22147E−1	0.22147E−1

Results for a uniform mesh with equally spaced nodes shown for reference.

Table 2
Discrete L_2 error as a function of element distortion for square plate example at $f = 500$ Hz, and $h = 1.0$ cm

Δ (h)	Element type			
	SRI4	MITC4	MLS4-ave	MLS4-local
0	0.183E0	0.183E0	0.2215E−1	0.2215E−1
0.05	0.273E0	0.185E0	0.2218E−1	0.2220E−1
0.10	0.800E0	0.190E0	0.2223E−1	0.2229E−1
0.15	0.826E+1	0.198E0	0.2255E−1	0.2246E−1
0.20	0.150E+1	0.210E0	0.2352E−1	0.2278E−1

Table 3
Discrete L_2 error as a function of element distortion for square plate example at $f = 500$ Hz, and $h = 0.5$ cm

Δ (h)	Element type			
	SRI4	MITC4	MLS4-ave	MLS4-local
0	0.348E−1	0.348E−1	0.7892E−2	0.7892E−2
0.05	0.492E−1	0.350E−1	0.7986E−2	0.7948E−2
0.10	0.976E−1	0.356E−1	0.8277E−2	0.8127E−2
0.15	0.201E0	0.367E−1	0.8789E−2	0.8436E−2
0.20	0.433E0	0.383E−1	0.9551E−2	0.8890E−2

that MLS4 is superior to both the underlying MITC4 element and the SRI4 element Fig. 12.

We next study the solution on a quasi-uniform mesh of distorted elements generated with the 'free-mesh' quadrilateral element algorithm used in the commercial CAE software package I-DEAS from Structural Dynamics Research Corporation (SDRC). Fig. 13 shows a typical mesh of regular quadrilateral elements generated with the automatic mesh algorithm with average element length $h_{\text{ave}} = (A/N_{\text{T}})^{1/2} = 0.936$. Fig. 13 shows the vertical deflection along the diagonal line of symmetry parameterized by coordinate $s = ((x-50)^2 + (y-50)^2)^{1/2}$. Results for SRI4 and MITC4 show large errors in the solution. In contrast, the MLS4 element solution closely matches the analytical solution. Table 4 shows results for 'free-meshes' with average element size ranging from 1.257 to 0.741. Again we observe large improvement in accuracy using the MLS4 element compared to the MITC4 element for quasi-uniform meshes with distorted elements. The discrete L_2 error for the MLS4-local solution, with mesh size $h = \sqrt{A_e}$ used in the definition for mesh parameters r_1, r_2, is reduced significantly over the underlying MITC4 element. Interestingly, for the 'free-meshes' studied here, the MLS4-ave solution, with an average element size $h_{\text{ave}} = \sqrt{A/N_{\text{T}}}$ defined over the total mesh, further reduces the error compared to MLS4-local.

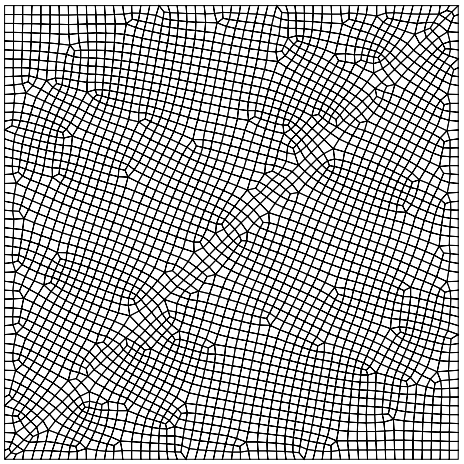

Fig. 12. Typical distorted mesh with average element size $h_{\text{ave}} = 0.936$, generated with SDRC I-DEAS 'free-mesh' quad element algorithm.

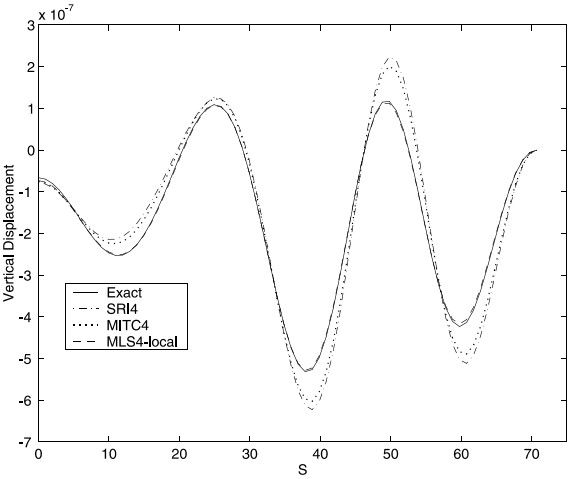

Fig. 13. Vertical deflection along the diagonal line of symmetry using the 'free-mesh' shown in Fig. 12. Frequency $f = 500$ Hz.

Table 4
Discrete L_2 error for square plate example at $f = 500$ Hz. 'Free-meshes' generated with I-DEAS quad element generator

h_{ave}	Element type			
	SRI4	MITC4	MLS4-ave	MLS4-local
1.257	0.61037E0	0.37244E0	0.43420E−1	0.72982E−1
1.115	0.29672E0	0.22830E0	0.32593E−1	0.42995E−1
0.936	0.18847E0	0.14724E0	0.92567E−2	0.12893E−1
0.741	0.95188E−1	0.74687E−1	0.37013E−2	0.43777E−2

6.1.3. Nonuniform meshes

Finally, we study the performance of our MLS4 element for nonuniform meshes composed of fine and course mesh regions with transition. For nonuniform meshes, the finite element approximation will exhibit errors from both numerical dispersion and reflection

errors resulting from transitions in mesh size [53]. We construct the meshes from a surface bisecting the plate along the diagonal line of symmetry. We then define a 'free-mesh' of similarly sized regular elements within this region, and then transition to a course mesh in the surrounding off-diagonal surfaces. Fig. 14 shows a typical mesh composed of the two resulting patches with transition—Patch 1 with a relatively course mesh, and Patch 2 with a fine mesh. Fig. 15 shows a sequence of nonuniform meshes with course to fine mesh transition.

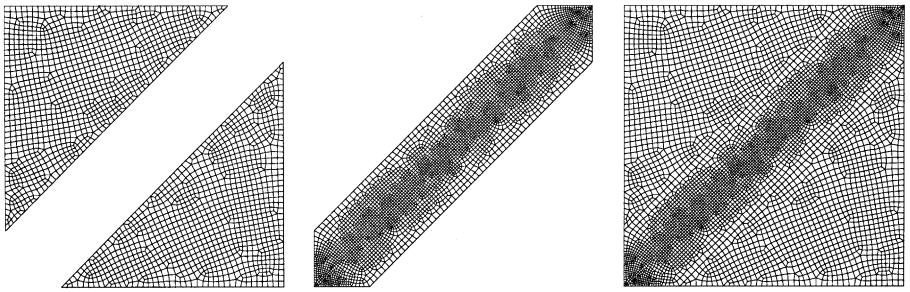

Fig. 14. Mesh 3 composed of two patches of similarly sized elements. Left: Patch 1, $h_{\text{ave}}^{(1)} = 0.895$. Center: Patch 2, $h_{\text{ave}}^{(2)} = 0.506$, Right: Total, $h_{\text{ave}} = 0.673$.

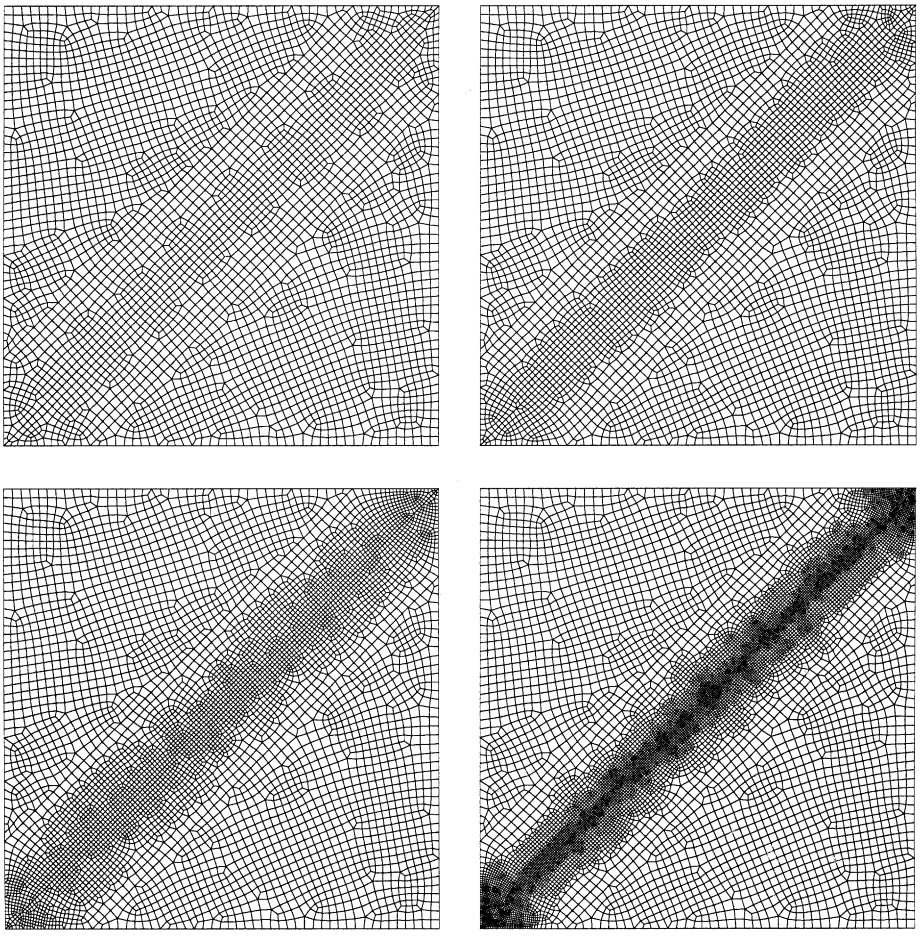

Fig. 15. Nonuniform meshes denoted Mesh 1 thru Mesh 4 for simply supported Mindlin plate model. Average element sizes are given in Table 5.

Table 5
Nonuniform meshes for square plate example showing average element size over Patches 1 and 2, denoted $h_{ave}^{(1)}$ and $h_{ave}^{(2)}$, and average size over the total mesh, denoted h_{ave}

Mesh	Average element size		
	$h_{ave}^{(1)}$	$h_{ave}^{(2)}$	h_{ave}
1	0.895	0.825	0.867
2	0.895	0.682	0.797
3	0.895	0.506	0.673
4	0.895	0.319	0.480

The first mesh (Mesh 1) has a small change in mesh size, whereas the last mesh (Mesh 4) has a very large mesh transition. The average element sizes for these nonuniform meshes are given in Table 5. We consider three alternative methods for computing the element size h used in the mesh parameters r_1 and r_2 for our MLS4 element. The first two definitions are the same as used earlier; average element size h_{ave}, computed over the total mesh, and local element size $h_e = \sqrt{A_e}$ computed from the square root of the element area. In addition, we consider the element size h to be an average over the two different patches of similarly sized elements. With this definition, elements in Patch 1 are assigned a value $h_{ave}^{(1)}$, and elements in Patch 2 are assigned a different value $h_{ave}^{(2)}$. Table 6 compares the relative discrete L_2 error for the competing plate elements using the different nonuniform meshes shown in Fig. 15. The results from this study and other nonuniform mesh gradings (not shown) exhibit no significant deterioration in performance due to mesh transitions for our MLS4 plate element. Interestingly, an average size over a patch of similarly sized elements gave better results compared to the local element based definition. This result suggests that improved performance may be obtained using an average element size for h in the mesh parameter definitions, when meshes are constructed from 'free-mesh' distributions of regular elements over patches of similarly sized elements, as typically generated with commercial mesh algorithms such as those available in I-DEAS. However, when distinct patches of elements are not present in the mesh, the local element size definition remains the most robust, leading to a predictable and significant reduction in error compared to the underlying MITC4 element.

7. Conclusions

Low-order quadrilateral plate elements such as the MITC4 mixed interpolation element [9], while eliminating shear locking problems for thin plates, exhibit poor accuracy for both real propagating and imaginary decaying wave number components at intermediate to high frequencies. By selecting mesh parameters in a generalized least-squares operator to match (for a given wave angle) exact wave number–frequency relations for Mindlin plates, dispersion accuracy is increased by a factor of three over the underlying MITC4 element, with trivial extra cost. The extra cost is proportional to solving a quadratic equation for the mesh parameters in closed form for each element. This is a reduction in cost compared to a similar least-squares stabilization operator applied to the Hellinger–Reissner functional for assumed stress plate elements—in that context, solution of a cubic equation was required [30]. As a general rule of thumb, the mesh resolution requirements to obtain a 1.5% dispersion error are reduced from 20 to 10 elements/wavelength. An important property of our MLS4 four-node quadrilateral plate element is that in the zero frequency limit, the mesh parameters vanish, thus recovering the shear-locking behavior of the underlying MITC4 element. The property of field consistency in the MITC transverse shear strain interpolation simplifies the residuals appearing in the generalized least-squares operators, and leads to a simple modification of the element dynamic stiffness matrix. From numerical studies of wave number accuracy, the choice of $\varphi = 30°$ in the definition for the mesh parameters maximizes the dispersion accuracy over all possible wave angle directions.

While optimally designed for uniform meshes, results from both dispersion analysis and numerical examples show that our MLS4 element improves the accuracy of the underlying MITC4 element for quasi-uniform parametric meshes and distorted meshes generated with automatic 'free-mesh' generators. When meshes are constructed from 'free-mesh' distributions of regular elements over patches of similarly sized elements, the numerical results showed increased performance using an average element size for each element patch in the definitions for the mesh parameters. However, when distinct patches of similarly sized elements cannot be

Table 6
Discrete L_2 error for nonuniform meshes for square plate example at $f = 500$ Hz

Mesh	Element type				
	SRI4	MITC4	MLS4-ave	MLS4-patch	MLS4-local
1	0.15964E0	0.11716E0	0.10531E−1	0.10037E−1	0.17081E−1
2	0.15683E0	0.10885E0	0.13062E−1	0.09246E−1	0.17959E−1
3	0.15197E0	0.10197E0	0.31230E−1	0.10069E−1	0.15652E−1
4	0.16184E0	0.10269E0	0.37237E−1	0.13544E−1	0.15969E−1

identified in the nonuniform mesh, a local element size definition gives the most robust solution, leading to a predictable and significant reduction in error compared to the underlying MITC4 element.

Further improvements we are investigating include the combination of shear stabilization methods with the mixed interpolation technique of the original MITC elements given in [27], as a basis for developing generalized least-squares operators for improved dynamic wave response. Further extensions of the generalized least-squares methods developed here for plate elements include generalizations to curved shell elements with bending-membrane coupling.

Acknowledgements

Support for this work was provided by the National Science Foundation under grant CMS-9702082 in conjunction with a Presidential Early Career Award for Scientists and Engineers (PECASE), and is gratefully acknowledged.

References

[1] Thompson LL, Thangavelu SR, A stabilized MITC finite element for accurate wave response in Reissner–Mindlin plates. In: Bathe KJ, editor. Computational fluid and solid mechanics, Proceedings, First MIT Conference on Computational Fluid and Solid Mechanics. Elsevier Science Ltd.; 12–15 June 2001. p. 502–8.

[2] Graff KF. Wave motions in elastic solids. New York: Dover Publications; 1975.

[3] Magrab EB, Vibrations of elastic structural members. Sijthoff and Noordhoff, 1979.

[4] Reissner E. On the theory of bending of elastic plates. J Mathematical Phys 1944;23:184–91.

[5] Reissner E. The effect of transverse shear deformation on the bending of elastic plates. ASME J Appl Mech 1945;12:69–77.

[6] Mindlin RD. Influence of rotatory inertia and shear on flexural motions of isotropic, elastic plates. ASME J Appl Mech 1951;18:31–8.

[7] Hughes TJR, Cohen M, Haroun M. Reduced and selective integration techniques in the finite element analysis of plates. Nucl Eng Des 1978;46:203–22.

[8] Tezduyar TE, Hughes TJR. Finite elements based on Mindlin plate theory with particular reference to the four-node bilinear isoparametric element. ASME J Appl Mech 1981;46:587–96.

[9] Bathe KJ, Dvorkin E. A four node plate bending element based on Mindlin–Reissner plate theory and mixed interpolation. Int J Numer Meth Eng 1985;21:367–83.

[10] Prathap G, Somashekar BR. Field- and edge-consistency synthesis of a 4-noded quadrilateral plate bending element. Int J Numer Meth Eng 1988;26:1693–708.

[11] Aminpour MA. An assumed-stress Hybrid-node shell element with drilling degrees of freedom. Int J Numer Meth Eng 1992;33:19–38.

[12] Aminpour MA. Direct formulation of a hybrid 4-node shell element with drilling degrees of freedom. Int J Numer Meth Eng 1992;35:997–1013.

[13] Bramble JH, Sun T. A negative-norm least squares method for Reissner–Mindlin plates. Mathematics Computat 1998;67:901–16.

[14] Hughes TJR, The finite element method. Englewood Cliffs, NJ: Prentice-Hall; 1987.

[15] Bathe KJ. Finite element procedures. Englewood Cliffs, NJ: Prentice-Hall; 1996.

[16] Bathe KJ, Brezzi F. On the convergence of a four-node plate bending element based on Mindlin/Reissner plate theory and mixed interpolation. In: Whiteman JR, editor. Proc Conf Math Finite Elements Appl V. New York: Academic press; 1985. p. 491–503.

[17] Bathe KJ, Brezzi F. A simplified analysis of two plate bending elements—the MITC4 and MITC9 elements. In: Pande GN, Middleton J, editors. Proc Int Conf Numer Meth Eng, (NUMETA 87). Dordrecht: Martinus Nijhoff; 1987.

[18] Bathe KJ, Bucalem ML, Brezzi F. Displacement and stress convergence of our MITC plate bending elements. Eng Comput 1990;7:291–302.

[19] Simo JC, Hughes JR. On the variational foundations of assumed strain methods. J Appl Mech 1986;53:51–4.

[20] Hughes TJR, Franca LP. A mixed finite element method formulation for Reissner–Mindlin plate theory: uniform convergence of all higher-order spaces. Comput Meth Appl Mech Eng 1988;67:223–40.

[21] Pitkaranta J. Analysis of some low-order finite element schemes for Mindlin–Reissner and Kirchhoff plates. Numer Math 1888;53:237–54.

[22] Arnold D, Falk R. A uniformly accurate finite element method for the Reissner–Mindlin plate. SIAM J Numer Anal 1989;26:1276–90.

[23] Brezzi F, Fortin M, Stenberg R. Error analysis of mixed-interpolated elements for Reissner–Mindlin plates. Math Models Meth Appl Sci 1991;1:125–51.

[24] Duran R, Liberman E. On mixed finite element methods for Reissner–Mindlin plate models. Math Comp 1992;58:561–73.

[25] Ibrahimbegovic A. Quadrilateral finite elements for analysis of thick and thin plates. Comput Meth Appl Mech Eng 1993;110:195–209.

[26] Arnold D, Falk R. Analysis of a linear-linear finite element for the Reissner–Mindlin plate model. Math. Models Meth Appl Sci 1997;7:217–38.

[27] Lyly M, Stenberg R. The stabilized MITC plate bending elements. Proc Fourth World Conference on Computational Mechanics. Buenos Aires, June 29–July 2, 1998.

[28] Benoit C, Coorevits P, Pelle J-P. Error estimation for plate structures: application using the DKT element. Eng Computat 1999;16(5):584–600.

[29] Thompson LL, Tong Y. Hybrid least squares finite element methods for Reissner–Mindlin plates. Proc ASME Noise Control and Acoustics Division—1999. 1999 ASME International Mechanical Engineering Congress and Exposition, ASME, NCA-vol. 26. 1999. p. 77–89.

[30] Thompson LL, Tong Y. Hybrid least squares finite element methods for Reissner–Mindlin plates. Comput Meth Appl Mech Eng, in press.
[31] Thompson LL, Thangavelu SR, Mixed least squares finite element methods for accurate wave response in Reissner–Mindlin plates. Technical Report, CMCU-00-02, Advanced Computational Mechanics Laboratory, Clemson University, August 2000.
[32] Thompson LL, Sankar S. Dispersion analysis of stabilized finite element methods for acoustic fluid interaction with Reissner–Mindlin plates. Int J Numer Meth Eng 2001;50(11):2521–45.
[33] Hughes TJR, Franca LP, Hulbert GM. A new finite element formulation for computational fluid dynamics: VIII. The Galerkin least squares method for advective-diffusive equations. Comp Meth Appl Mech Eng 1989;73:173–89.
[34] Shakib F, Hughes TJR, Johan Z. A new finite element formulation for computational fluid dynamics: X. The compressible Euler and Navier–Stokes equations. Comp Meth Appl Mech Eng 1991;89:141–219.
[35] Franca LP, Dutra do Carmo DG. The Galerkin gradient least-squares method. Comput Meths Appl Mech Eng 1989;74:44–54.
[36] Hughes TJR. Multiscale phenomena: Green's functions, the Dirichlet-to-Neumann formulation, subgrid scale models, bubbles and the origins of stabilized methods. Comput Meth Appl Mech Eng 1995;127:387–401.
[37] Hughes TJR, Feijoo GR, Mazzei Lucas, Quincy Jean-Baptiste. Variational multiscale method—a paradigm for computational mechanics. Comput Meths Appl Mech Eng 1998;166:3–24.
[38] Harari I, Hughes TJR. Finite element methods for the Helmholtz equation in an exterior domain: Model problems. Comp Meth Appl Mech Eng 1991;87:59–96.
[39] Harari I, Hughes TJR. Galerkin/least-squares finite element methods for the reduced wave equation with non-reflecting boundary conditions in unbounded domains. Comp Meth Appl Mech Eng 1992;98:411–54.
[40] Thompson LL, Pinsky PM. A Galerkin least squares finite element method for the two-dimensional Helmholtz equation. Int J Numer Meth Eng 1995;38:371–97.
[41] Harari I, Grosh K, Hughes TJR, Malhotra M, Pinsky PM, Stewart JR, Thompson LL. Recent developments in finite element methods for structural acoustics. Arc Computat Meth Eng 1996;3:132–311.
[42] Oberai AA, Pinsky PM. A residual-based finite element method for the Helmholtz equation. Int J Numer Meth Eng 2000;49(3):399–419.
[43] Ihlenburg F, Finite element analysis of acoustic scattering. Applied Mathematical Sciences, vol. 132. Springer; 1998.
[44] Franca LP, Macedo AP. A two-level finite element method and its application to the Helmholtz equation. Int J Numer Meth Eng 1998;43:23–32.
[45] Grosh K, Pinsky PM. Galerkin generalized least squares methods for Timoshenko beams. Comp Meth Appl Mech Eng 1996;132:1–16.
[46] Thompson L, Pinsky PM. Complex wave number Fourier analysis of the p-version finite element method. Computat Mech 1994;13(4):255–75.
[47] Malvern LE. Introduction to the mechanics of continuous medium. Englewood Cliffs, NJ: Prentice-Hall; 1969.
[48] Raviart PA, Thomas JM. A mixed finite element method for second order elliptic problems. Mathematical Aspects of the Finite Element Method. Lecture notes in math, vol. 606. Springer-Verlag; 1977. p. 292–315.
[49] Prathap G. The displacement-type finite element approach—From art to Science. Prog Aerospace Sci 1994; 30:295–405.
[50] Prathap G. Field-consistency approach to plate elements. Struct Eng Mech 1997;5(6):853–65.
[52] Mullen R, Belytschko T. Dispersion analysis of finite element semidiscretizations of the two-dimensional wave equation. Int J Numer Meth Eng 1982;18:11–29.
[53] Bazant ZP. Spurious reflection of elastic waves in nonuniform finite element grids. Comput Meth Appl Mech Eng 1978;16:91–100.